Time-lapse geophysical responses of hydrogen-saturated rock: Implications on subsurface monitoring

Chao Li[a], Shuvajit Bhattacharya[a], Muhammad M. Alhotan[b], Mojdeh Delshad[b]

[a]Bureau of Economic Geology, The University of Texas at Austin
[b]Hildebrand Department of Petroleum and Geosystems Engineering, The University of Texas at Austin

[1]To whom correspondence should be addressed. Email: Chao.li@beg.utexas.edu;

shuvajit.bhattacharya@beg.utexas.edu

Time-lapse geophysical responses of hydrogen-saturated rock: Implications on subsurface monitoring

Chao Li[a], Shuvajit Bhattacharya[a], Muhammad M. Alhotan[b], Mojdeh Delshad[b]

[a]Bureau of Economic Geology, The University of Texas at Austin
[b]Hildebrand Department of Petroleum and Geosystems Engineering, The University of Texas at Austin

Chao.li@beg.utexas.edu

Corresponding author: shuvajit.bhattacharya@beg.utexas.edu

ABSTRACT

Rock physics modeling and time-lapse geophysical modeling are effective methods to better understand the influence of hydrogen on rock properties and visualize hydrogen plume distribution and its migration direction. We study rock physics responses of hydrogen in a wedge model and a small field test scenario under different injection conditions. In doing so, we develop and test an integrated workflow that uses geologic data and dynamic flow simulation of H_2 plume migration to simulate corresponding time-lapse geophysical responses, namely, surface (prestack and poststack), cross-hole seismic, and electrical resistivity tomography (ERT) responses. Results from this study will help design effective time-lapse monitoring surveys, in terms of parameter including optimal rate/amount of H_2 injection, survey geometry, sensor locations. We investigate the influence of signal-to-noise ratio (SNR), injection location, lithology, permeability, and residual gas saturation on hydrogen monitoring. The choice of rock physics models has a profound impact on the resultant simulations that one can use to effectively design the monitoring surveys.

INTRODUCTION

Hydrogen storage in the subsurface is a viable option for energy supply and decarbonization.

(Shuster et al., 2021; Heinemann et al. 2021). Hydrogen storage in the depleted reservoirs, gas storage fields, and salt caverns has gained much of attention in North America and Europe. The suitability of a formation for safe and secure hydrogen storage depends on its porosity, permeability, reactive nature of the rock (and cement), integrity of the confining rocks, and fluid characteristics.

Monitoring time-lapse geophysical responses of hydrogen-saturated rock is essential for ensuring safety, efficiency, and environmental compliance in hydrogen storage projects (Zivar et al., 2021). This monitoring becomes challenging, especially in the case of subsurface hydrogen storage, as it presents unique technical challenges, in terms of hydrogen's high buoyancy, diffusion, potential reactions with rocks, well casing, and cement, and leakage. Therefore, the practical experimentation for long-term geological hydrogen storage is still limited (Abdellatif et al., 2023; Chabab et al., 2020; Zeng et al., 2022).

Pfeiffer et al. (2016) conducted a numerical geophysical monitoring for a porous media hydrogen storage at a synthetic heterogeneous field site via full waveform inversion (FWI), ERT, and gravity methods, successfully revealing the subsurface variations. Yang et al. (2024) proposed a new method to monitor underground hydrogen storage migration and distribution using acoustic full waveform inversion and got promising results. Faud et al. (2023) analyzed the seismic responses of hydrogen-bearing sandstone and demonstrated its implication for natural hydrogen exploration and storage. Furthermore, with the increasing popularity of deep learning (DL) in seismic exploration, Gao et al. (2024) developed a DL-based method for hydrogen leakage monitoring by associating the seismic response differences with velocity changes caused by hydrogen and produced satisfactory results. Later, Zhang and Li (2024) illustrated the role of geophysics in geologic hydrogen resources and indicated that multi-geophysical methods, efficient data acquisition, and machine learning in geologic hydrogen help to pursue research in the future.

Li and Bhattacharya (2024) presented preliminary results from rock physics modeling of a hydrogen-nitrogen-brine saturated rock; however, the study lacks various geologic and operational controls on hydrogen plume movement and corresponding geophysical responses.

In this study, we develop a rock-physics model for hydrogen-saturated rock and analyze the influence of hydrogen on both poststack and prestack synthetic seismic data (a wedge model) in the presence of diffusion effect. We then analyze the effects of different brine and hydrogen saturation and lithology on the seismic velocity of rocks. Furthermore, we test a generalized workflow for time-lapse multi-physics forward modeling that integrates geology, rock physics, and reservoir simulation from a potential reservoir for small-scale hydrogen storage. Bhattacharya et al. (2024) developed and tested the workflow in a carbon sequestration site. We compare and contrast results from surface seismic (poststack and prestack), crosshole ERT, and crosshole seismic under various hydrogen injection scenarios and signal-to-noise ratio (SNR). The hydrogen injection scenarios include: injection at the bottom of the reservoir, different realization of permeability and residual gas saturations, and injection at the middle of the reservoir. Multiple simulations demonstrate the influence of permeability, residual saturation, injection depth position, and varying SNR at the field setting on hydrogen monitoring.

Effective acquisition and interpretation of 4D geophysical data is hard in the field setting due to various challenges, including uncertainties in rock physics, co-locating 4D datasets due to survey and source/receiver configurations, spatial position, ground conditions, timing, wavelet phase, amplitude, and SNR. Not all time-lapse monitoring data are optimally collected and useful. Therefore, we need to plan properly and in advance to collect meaningful 4D geophysical data effectively. We expect our proposed workflow along with published programing codes will help to an extent.

The paper is organized as follows. In the methodology section, we first introduce the rock physics to generate the Vp, Vs, and density models for hydrogen-saturated rocks. Next, we review seismic and ERT modeling theory for further analysis. Finally, we test the integrated reservoir simulation-to-geophysical modeling workflow to analyze the influence of hydrogen on subsurface media in a geologic setting.

THEORY AND METHODOLOGY

Elastic properties estimation of hydrogen-saturated rocks and model boundary conditions

We adopt a rock physics model used to describe hydrogen's influence on porous rocks to describe the property changes caused by hydrogen. We use Madagascar (Fomel et al., 2013) and Matlab 2023b for rock physics modeling and seismic simulation (codes are in the appendix). Note that our model does not consider the complex interactions among hydrogen, brine, rock matrix, and cement (including microbial consumption). We assume that the rock matrix is isotropic and the pore network within the rock is fully connected. Moreover, we also assume that hydrogen and the in-situ brine comprise a two-phase fluid saturation. We do not use nitrogen (commonly used as a cushion gas for efficient production of injected gas) in the rock physics model. Let denote S_{brine}, and S_{H2} as the saturation of brine and hydrogen, where $S_{\text{brine}} + S_{\text{H2}} = 1$.

According to the theory of rock physics, we can calculate the effective bulk modulus, shear modulus, and density of the fluid-saturated medium to estimate the properties of the rocks. For mineral grain, the bulk modulus and shear modulus can be determined by the Voigt-Reuss Hill (VRH) average model (Hill, 1952) as

$$K_{\text{Voigt}} = \sum_{i=1}^{n} f_i K_i, \tag{1}$$

$$K_{\text{Reuss}} = \sum_{i=1}^{n} (f_i / K_i)^{-1}, \tag{2}$$

$$K_{\mathrm{VRH}} = \frac{1}{2}\left(K_{\mathrm{Voigt}} + K_{\mathrm{Reuss}}\right), \tag{3}$$

$$\mu_{\mathrm{Voigt}} = \sum_{i=1}^{n} f_i\, \mu_i\ , \tag{4}$$

$$\mu_{\mathrm{Reuss}} = \sum_{i=1}^{n} (f_i/\mu_i)^{-1}, \tag{5}$$

$$\mu_{\mathrm{VRH}} = \frac{1}{2}\left(\mu_{\mathrm{Voigt}} + \mu_{\mathrm{Reuss}}\right), \tag{6}$$

where n is the total number of mineral types. f_i, K_i, and μ_i represent the volume fractions, bulk modulus, and shear modulus of the *i*th mineral constituent.

Then, we adopt Hertz–Mindlin contact theory (Mindlin, 1949) and Hashin–Strikman (H-S) lower bound (Hashin and Shtrikman, 1963) to estimate the elastic modulus of dry rock matrix. Specifically, the dry rock frame modulus K_{dry} and μ_{dry} can be expressed as

$$K_{\mathrm{c}} = \left[\frac{C^2(1-\phi_c)^2\mu_{\mathrm{VRH}}^2 P_{\mathrm{eff}}}{18\pi^2(1-\nu)^2}\right]^{\frac{1}{3}}, \tag{7}$$

$$\mu_{\mathrm{c}} = \frac{5-4\nu}{10-5\nu}\left[\frac{3C^2(1-\phi_c)^2\mu_{\mathrm{VRH}}^2 P_{\mathrm{eff}}}{2\pi^2(1-\nu)^2}\right]^{\frac{1}{3}}, \tag{8}$$

$$\xi = \frac{\mu_{\mathrm{c}}}{6}\left(\frac{9K_c+8\mu_c}{K_c+2\mu_c}\right), \tag{9}$$

$$K_{\mathrm{dry}} = \left[\frac{\phi/\phi_c}{K_c+4\mu_c/3} + \frac{1-\phi/\phi_c}{K_{\mathrm{VRH}}+4\mu_c/3}\right]^{-1} - \frac{4}{3}\mu_c, \tag{10}$$

$$\mu_{\mathrm{dry}} = \left[\frac{\phi/\phi_c}{\mu_c+\xi} + \frac{1-\phi/\phi_c}{\mu_{\mathrm{VRH}}+\xi}\right]^{-1}, \tag{11}$$

where K_{c} and μ_{c} stand for the effective bulk and shear modulus of a dry, dense, random pack of identical spherical grains under critical porosity $\phi_c = 0.3$. $\mathrm{C} = 2.8/\phi_c$ is the average number of contacts per grain and ν is the grain Poisson's ratio. P_{eff} is the effective pressure. With the above rock physics parameters, we can calculate the saturated bulk and shear modulus K_{sat} and μ_{sat} via low-frequency Gassmann theory (Gassmann, 1951) and Brie mixing (Brie et al., 1995) are calculated, as follows

$$K_{\text{sat}} = K_{\text{dry}} + \frac{\left(1-\frac{K_{\text{dry}}}{K_{\text{VRH}}}\right)^2}{\left(\frac{\phi}{K_{\text{fl}}}+\frac{1-\phi}{K_{\text{VRH}}}-\frac{K_{\text{dry}}}{K_{\text{VRH}}^2}\right)}, \tag{12}$$

$$\mu_{\text{sat}} = \mu_{\text{dry}}, \tag{13}$$

$$K_{\text{fl}} = \left(K_{\text{brine}} - K_{H_2}\right)S_{\text{brine}}^{e} + K_{H_2}, \tag{14}$$

where K_{brine} and K_{H_2} denote the bulk modulus of brine and hydrogen. e is a patchiness exponent, ranging from 1 to 40. For instance, $e = 1$ represents patchy mixing, and $e = 40$ stands for uniform mixing. Commonly, the value of e is tuned to match the case for hydrogen-brine mixture.

Furthermore, the effective density of the hydrogen-brine saturated rocks can be estimated by

$$\rho_{\text{eff}} = (1-\phi)\rho_{\text{r}} + \phi\rho_{\text{fl}}, \tag{15}$$

$$\rho_{\text{fl}} = S_{H_2}\rho_{H_2} + S_{\text{brine}}\rho_{\text{brine}}, \tag{16}$$

where ρ_{r} is the density of the rock matrix. According to equations 12-16, the velocity of the hydrogen-brine saturated rocks can be calculated by

$$v_p = \left(\frac{K_{\text{sat}}+\frac{4}{3}\mu_{\text{sat}}}{\rho_{\text{eff}}}\right)^{\frac{1}{2}}, \tag{17}$$

$$v_s = \left(\frac{\mu_{\text{sat}}}{\rho_{\text{eff}}}\right)^{\frac{1}{2}}. \tag{18}$$

Note that v_{p} and v_{s} are determined by elastic modulus, and the density of rocks and hydrogen with different saturations will lead to the variations of velocities. Once we derive the elastic parameters (e.g., Vp, Vs, and density) of hydrogen-saturated reservoir, we can generate the corresponding seismic and ERT responses. More details will be illustrated in the next subsection.

Poststack and prestack seismic forward modeling for hydrogen-saturated rock

Poststack seismic responses $\boldsymbol{d}$ can be cast as the convolution between a wavelet and

reflectivity series (Robinson, 1967), which has the following expression

$$\boldsymbol{d} = \boldsymbol{W}\boldsymbol{r}, \tag{19}$$

where $\boldsymbol{W}$ is the wavelet convolution matrix and $\boldsymbol{r}$ represents the reflectivity series. Note that in the case of normal incidence, the reflectivity series can be calculated from the acoustic impedance (AI) using the following equation

$$\mathrm{AI}(t) = \mathrm{V_p}(t)\rho(t), \tag{20}$$

$$\mathrm{r}(t) = \frac{\mathrm{AI}(t+1)-\mathrm{AI}(t)}{\mathrm{AI}(t+1)+\mathrm{AI}(t)}. \tag{21}$$

Based on the rock physics model, we can get velocity and density and substitute them into equation 21, it is easy for us to get reflectivity series r(t) and convolve r(t) with a source wavelet to generate poststack seismic data using equation 19.

As for prestack amplitude versus angle (AVA) seismic response, we adopt a Zoeppritz approximation equation (Shuey, 1985), the reflection coefficient $R_{pp}(\theta)$ $(0 < \theta < 30^{\circ})$ can be written as

$$R_{pp}(\theta) = R_p + R_h \sin^2\theta, \tag{22}$$

$$R_p = \frac{1}{2}\left[\frac{\Delta v_p}{v_p} + \frac{\Delta\rho}{\rho}\right], \tag{23}$$

$$R_h = \left(R_p A_0 + \frac{\sigma_1-\sigma_0}{(1-\sigma)^2}\right), \tag{24}$$

$$A_0 = \frac{2\Delta v_p}{v_p R_p} - 2\left(1 + \frac{2\Delta v_p}{v_p R_p}\right)\frac{1-2\sigma}{1-\sigma}, \tag{25}$$

where R_p represents the zero-offset reflection coefficients for P wave and σ is Poisson's ratio of the subsurface media. It is noticeable that $R_{pp}(\theta)$ has a linear relationship with $\sin^2\theta$ and we can refer to R_p as the intercept and R_h as the gradient. Combining equations 22~25 with the rock physics model, we can analyze the influence of hydrogen on prestack reflection coefficients.

Diffusion effect on seismic responses

As discussed above, hydrogen has a high diffusivity, and can escape from reservoir to caprocks. Diffusion loss means the net movement of H_2 generally from a region of higher concentration to a region of lower concentration (e.g., from reservoir to confining layer), which the diffusion coefficient can parameterize. A larger diffusion coefficient means it is easier for gas to escape the reservoir and net loss of hydrogen which is not economical. The diffusion effect will influence the H_2 saturation of the confining layer and reservoir in the long-term. To estimate the influence of the diffusion effect on subsurface properties, the diffusion coefficient is integrated into the rock physics model, enabling an understanding of the behavior of the subsurface variations better. There are no equations incorporating the diffusion effect into the rock physics model yet, as it is a complex molecular dynamics phenomenon. We attempt to do it at a macro-scale.

Assuming the volume and porosity of confining layer and reservoir are $\mathrm{V_{con}}$, $\mathrm{V_{res}}$, ϕ_{con} and ϕ_{res}, then the total H_2 storage capacity of confining layer $\mathrm{M_{con}}$ can be expressed as

$$\mathrm{M_{con}} = \mathrm{V_{con}}\phi_{con}\rho_{H_2}. \tag{26}$$

When the storage capacity of confining layer reaches $\mathrm{M_{con}}$, it means that the hydrogen saturation $\mathrm{S_{H_2}^{con}}$ of confining layer will be 1. Therefore, for simplicity, the time-varying $\mathrm{S_{H_2}^{con}}$ has the following form

$$\mathrm{S_{H_2}^{con}}(t) = \frac{\mathrm{d_{coef}}tL}{\mathrm{M_{con}}}, \tag{27}$$

where $\mathrm{d_{coef}}$ represents the diffusion coefficient (e.g., ranging from 1×10^{-10} m^2/s to 6×10^{-8} m^2/s), which can be measured in the laboratory (Strauch et al., 2023; Borello et al., 2024). t represents time after injection and L is the cross-sectional area between the confining layer and reservoir.

As for the reservoir, due to the influence of diffusion, the corresponding hydrogen saturation

will decrease over time, and we can derive a time-varying saturation $S_{H_2}^{res}$ with the following form

$$S_{H_2}^{res}(t) = \frac{S_{H_2}^{ini} V_{res} \phi_{res} \rho_{H_2} - d_{coef} tL}{V_{res} \phi_{res} \rho_{H_2} S_{H_2}^{ini}}, \tag{28}$$

where $S_{H_2}^{ini}$ is the initial hydrogen saturation of reservoir. Equations 27 and 28 are the key steps to estimate the time-varying subsurface model. We can just incorporate the time-varying saturation of confining layer and reservoir to estimate the subsurface model over time and conduct poststack and prestack seismic analysis to evaluate the variation of seismic responses.

Theory of electrical resistivity tomography

In this part, we will briefly review the basic theory of ERT. ERT is a geophysical imaging technique used to map subsurface resistivity distribution by injecting electrical currents into the ground and measuring resulting voltage differences. Commonly, the potential voltage measurements at the surface do not directly represent the resistivity structure. Instead, inversion algorithms are used to reconstruct the subsurface resistivity model that best explains the observed data. Let denote d_{res} as the measured data and $\mathbf{m}$ as the subsurface resistivity model, then the subsurface resistivity model can be estimated by solving such as an objective function $\mathbf{p}$

$$\mathbf{p} = \frac{1}{2} \|\mathbf{F}(\boldsymbol{m}) - \boldsymbol{d}_{res}\|_2^2, \tag{30}$$

where operator $\mathbf{F}$ represents the forward modeling process. Given an initial subsurface resistivity mode $\mathbf{m_0}$, we can update the model in an iterative manner as follow

$$\mathbf{m}_{i+1} = \mathbf{m}_i + \Delta\mathbf{m}, \tag{31}$$

$$\left(\mathbf{J}^T \mathbf{W}_d^T \mathbf{W}_d \mathbf{J} + c\mathbf{R}\right)\Delta\mathbf{m} = -\mathbf{J}^T \mathbf{W}_d^T (\mathbf{F}(\boldsymbol{m}) - \boldsymbol{d}_{res}) - c\mathbf{R}\mathbf{m}, \tag{32}$$

where $\mathbf{J}$ is the Jacobian matrix, which can be estimated by conducting the derivative of measured data $\boldsymbol{d}_{res}$ with respect to resistivity model $\mathbf{m}$. $\mathbf{W_d}$ is a diagonal data weight matrix with values

$1/\sigma_i$, where σ_i is the standard deviation of measurement i. **R** is the roughness matrix, controlling the smoothness of the inverted result and c is the corresponding trade-off, which aims to mitigate the influence of noise during inversion process and lead to a more reliable result.

Theory of crosshole seismic forward modeling

Crosshole seismic forwarding is a commonly used method for subsurface monitoring, where the sources and receivers are set in the borehole. Based on the theory of wave equation, we can generate crosshole seismic responses. Usually, acoustic wave equation has the following form

$$\frac{1}{v^2}\frac{\partial u(\mathbf{x},t)}{\partial t^2} = -\nabla^2 u(\mathbf{x},t), \tag{33}$$

where v is the velocity, u(**x**,t) represent the wavefield, and S_{wav} is the source wavelet. Note that according to the low rank approximation scheme, the relationship between the adjacent time step can be expressed as

$$u(\mathbf{x},t+\Delta t) = \int \hat{u}(\mathbf{k},t)e^{i\phi(\mathbf{k},\mathbf{x},\triangle t)}d\mathbf{k}, \tag{34}$$

where **x** and **k** stand for spatial coordinates and wavenumber, $\hat{u}(\mathbf{k},t)$ is the spatial Fourier transform of $u(\mathbf{x},t)$, and $e^{i\phi(\mathbf{k},\mathbf{x},\triangle t)}$ represents the wavefield extrapolation matrix. To determine $e^{i\phi(\mathbf{k},\mathbf{x},\triangle t)}$ and implement wave propagation, we adopt a lowrank approximation scheme, which is more flexible and computationally efficient, and the detailed derivation can be found in Fomel et al. (2013). Once we get the propagation matrix, we can calculate wavefield slice at each time step and obtain the complete wavefield $u(\mathbf{x},t)$ by merging all the slices. Consequently, it is convenient for us to extract crosshole seismic responses from $u(\mathbf{x},t)$ based on the receiver's locations. Mathematically, such extraction process can be formed as

$$d_{cross} = \mathbf{E}u(\mathbf{x},t), \tag{35}$$

where d_{cross} is the corresponding crosshole seismic data and operator **E** works to extract signals

at receivers' locations.

RESULTS AND DISCUSSIONS

The influence of hydrogen on Vp, Vs, and density under different conditions

In this section, we use synthetic data and a pilot experiment at a proposed hydrogen injection site to demonstrate the influence of hydrogen on the subsurface media over time. Figure 1 shows the detailed workflow of rock physics forward modeling and the corresponding seismic simulation. Based on the properties of minerals (e.g., clay, quartz, and so on) and fluids (e.g. brine, hydrogen, and so on), we will first estimate the grain matrix modulus using the VRH average model. Then the soft sand model is incorporated to calculate the modules of the rock frame. Next, we apply the Gassmann substitution equation to calculate the effective modulus of hydrogen saturated rock. It is noticeable that when the diffusion effects are neglected, we can just use a constant hydrogen saturation for modeling. However, if diffusion effects are considered, we can estimate a time-varying hydrogen saturation for both confining layers and reservoir via equations 27 and 28 and then conduct poststack (e.g., equations 19-21)) and prestack (e.g., equations 22-25) modeling for further analysis.

Figure 2 shows the basic properties of hydrogen at T=35°C under different pressures, where we can see that both the velocity and density of hydrogen increase with increasing pressure. Hydrogen has a relatively high velocity and extremely low density, leading to different responses during geophysical monitoring. We first discuss the hydrogen influence on v_p, v_s, and ρ variations, respectively. Table 1 shows the parameters we use. In our experiment, the volume fraction ratio of clay and quartz as 1:7 assumed constant.

Table 1: Properties of minerals and fluids

Constituents	Bulk modulus, K (GPa)	Shear modulus, mu (GPa)	Density (g/cm^3)
Clay	21	6.85	2.6
Quartz	39	45	2.65
Brine	2.49	0	1.03
Hydrogen	0.015	0	0.0045

Figure 3 shows the velocity and density variation under different porosities and hydrogen saturations. We fix the patchiness exponent $e = 3$. Obviously, we can see that the v_p will decrease with the increasing hydrogen saturation. Specifically, v_p decreases more rapidly when the hydrogen saturation is less than 50% and then decreases slower, indicating that v_p is more sensitive to low hydrogen saturation. Moreover, v_p behaves negatively in correlation with porosity at a fixed saturation. As for v_s and ρ, we can see that they vary linearly with different hydrogen saturations. According to equation 18, the shear modulus remains unchanged, but the denominator decreases, leading to the increasing v_s. Figure 3c shows the variations of ρ. Although ρ shows a similar trend with the increasing hydrogen saturation under different porosities, it decreases more quickly when the porosity is higher, allowing the possibility of using ρ and v_p jointly to estimate hydrogen saturation.

Wedge model seismic responses influenced by hydrogen

Based on the influence of hydrogen on elastic parameters (e.g., velocity and density), we build a wedge model to further analyze the influence of hydrogen on seismic responses. Because hydrogen is more sensitive to v_p compared with v_s and ρ, here we will first focus on the variation of v_p induced by hydrogen on poststack data. A wedge model is created as shown in Figure 4,

where the confining layer is completely brine-saturated before hydrogen injection, the volume fraction ratio of clay and quartz as 9:1, and the porosities corresponding to the top and bottom layers are 8% and 4%. As for the reservoir, the porosity is 20%, the volume fraction ratio of clay and quartz as 1:7, and the temperature and pressure are 35°C and 6MPa. Moreover, the saturations corresponding to hydrogen, and brine are 40%, and 60%, respectively. Using the rock physics model, Figures 4b and 4c are the v_p models before and after hydrogen injection. The velocity in the reservoir decreases significantly from 2.7 km/s to 2.3 km/s, indicating a change of -15%. Similarly, we can estimate the density model before and after hydrogen injection and multiply density with velocity to build the acoustic impedance model as shown in Figures 5a and 5b. Without considering diffusion and leakage of hydrogen from the reservoir to the confining layer, there are no apparent changes in the confining layers. Accordingly, we can generate poststack seismic data based on equations 19-21 with a 60 Hz source wavelet. Figures 5c and 5d are the generated seismic data before and after hydrogen injection. Noticeably, that the reflection seismic amplitude between the confining rock and reservoir increase a lot. The injected hydrogen dramatically decreases the reservoir velocity and density, leading to an increasing impedance difference at the top and bottom interfaces of the reservoir. Therefore, the reflection amplitude at the top and bottom interfaces will increase, which means that hydrogen injection can cause a bright spot on the poststack seismic profile, which can indicate hydrogen.

Effect of diffusion on seismic response in the wedge model

Furthermore, based on the experiment above, The impact of the diffusion influence on hydrogen storage is investigated. Using equations 26-28, time-varying hydrogen saturation for both confining layers and reservoir at a fixed time are calculated. Then the time-varying subsurface models substituted in time-varying saturations into the rock physics modeling framework are

calculated. The initial hydrogen saturation is assumed to be 40% (e.g., 1.25×10^5 kg hydrogen injected), and the diffusion coefficient is 2×10^{-8} m^2/s (Borello et al. 2024). Figure 6 shows the synthetic monitoring results over time, and it is evident that due to the influence of diffusion, hydrogen will move from the reservoir to the confining layers. Consequently, the velocity of the confining layer will decrease from 2.82 km/s to 2.79 km/s, and the velocity of the reservoir will increase gradually from 2.28 km/s to 2.35 km/s. The confining layer and reservoir velocity variation rates are -1% and 3%, respectively. To intuitively demonstrate diffusion influence on seismic data, we use a similar scheme to generate time-varying impedance model and the corresponding seismic data as shown in Figure 7, the impedance of the confining layer and the impedance of the reservoir show tiny difference. Based on the time-varying impedance models, we then estimate the reflectivity series and convolve them with a 60 Hz source wavelet to synthesize seismic responses. With the increasing time, we see that the seismic responses at the top interface of the reservoir are almost unchanged. Therefore, diffusion may not be a significant concern in monitoring, especially in case of cyclic injection and production of hydrogen, where it might be difficult to determine such small-scale changes.

We show prestack seismic responses before and after hydrogen injection under different porosities and saturations in Figure 8. The confining rock is assumed impermeable and equations 22-25 are used to calculate the reflection coefficient versus incident angle from 0° to 30°, for fixed hydrogen saturation in the range of 0% to 70%. The top left panel in Figure 8 is the estimated $R_{pp}(\theta)$ under $\phi = 20\%$, the results indicate that with the increasing incident angle, $R_{pp}(\theta)$ will decrease, especially for larger incident angle (e.g., $\theta > 15^\circ$). The top right panel in Figure 8 is the calculated reflection coefficients under $\phi = 30\%$. Note that when porosity increases, the hydrogen decreases the impedance of the reservoir with respect to that of the confining rock, resulting in

more negative reflection coefficients for normal incidence compared with those of $\phi = 20\%$. To provide an intuitive comparison, we extract single curve at different S_{H2} (e.g., 10%, 20%, and 30%) and the results are displayed in the bottom panels of Figure 8. The three curves show similar descent trends. Specifically, beginning from -0.07, $R_{pp}(\theta)$ increases negatively and such case corresponds to the AVA class III (Castagna et al., 1998). The bottom right panel of Figure 8 shows the reflection coefficient variations under variable hydrogen saturations when $\phi = 30\%$. Note that the reflection coefficient at $\theta = 0^{\circ}$ is more negative and the curves show a flat trend, indicating weak AVA when porosity increases. We can find that AVA characterization will concentrate at class IV in the case of $\phi = 30\%$.

Moreover, the saturation state (uniform vs. patchy) of hydrogen will also affect the AVA response. As we mentioned above, the saturation state can be determined by patchiness exponent e in equation 14 (e.g., $e = 1$ for patchy saturation and $e = 40$ for uniform saturation). We fix $\phi = 20\%$ and then estimate the reflection coefficients under different conditions, and the results are displayed in Figure 9. It is clear that when S_{H2} is low (e.g., less than 20%), AVA will be close to class II under patchy saturation and convert to class III gradually with the increasing S_{H2}. In addition, we can also see that $R_{pp}(\theta)$ will increase negatively at low S_{H2} with increasing patchiness, which demonstrates that AVA is close to class II or class III under uniform saturation. Similar to poststack seismic response, prestack AVA will also be influenced by diffusion effect. Therefore, using the same parameter as the poststack experiment, the time-varying AVA responses are calculated at the top interface of the wedge model at Distance=750 m after hydrogen injection. Figure 10 shows the time-lapse AVA over time, where we can see that the reflectivity becomes larger after injection and increases negatively with the increasing incident angle. Influenced by the diffusion effect, the blue curve moves towards the AVA response before injection (red). Notably,

although the amplitude of AVA will get smaller than the AVA response after injection over time, it still concentrates in class III. Based on Figures 6, 7, and 10, we can find that the injected hydrogen has significant influences on seismic responses, and the influence of diffusion is very limited (e.g., about 7.6% hydrogen loss after 10 years).

Effect of lithology on rock physics response in the wedge model

We also investigate the influence of lithology on the velocity variation under different hydrogen saturations. In the first case, we assume that the reservoir is a clean sandstone (100% quartz) and saturated with hydrogen and brine and then change the hydrogen saturation sequentially to estimate the velocity by performing fluid substitution. Then we introduce heterogeneity in the reservoir by adding a clay fraction of 25%, i.e., the ratio between clay and quartz being 1:3. We use the same workflow to calculate the corresponding velocity at different hydrogen saturations (Figure 11). Increasing hydrogen saturation will decrease the velocity significantly in both experiments. By comparing the blue curves in both experiments (100% brine), we can see that if we increase the clay fraction, the velocity of the reservoir will decrease more due to both lithology and fluid effect.

Dynamic reservoir simulation-guided geophysical modeling

In this section, we discuss five synthetic simulation cases of a small volume of hydrogen injection in a sandstone reservoir, which could be used as a potential field test. In the model, the reservoir is gently dipping and unfaulted. For all cases, the temperature of reservoir is about 35°C, and the pressure is 4.5 MPa. Moreover, we set the porosities of top layers, reservoir, and bottom layers are 8%, 20%, and 4%, respectively. The clay fractions of top layers, reservoir, and bottom layers are 90%, 0%, and 90%. To make the modeling more realistic, we consider the effects of solubility, diffusion, vaporization, and hysteresis and the corresponding saturation models are

created by CMG-GEM software (Machado et al., 2024).

The synthetic cases aim to determine the key factors of hydrogen storage from different perspectives (e.g., permeability, residual gas saturation, injection position as well as SNR). Tables 2 and 3 show some basic parameters used for the experiments and the key difference of each experiment.

Table 2. Basic parameters of the numerical experiments

Parameters	**Most likely values**
Dip angle	2.5 deg
Permeability, md	50 mD
Residual Water Saturation	0.24
Kv/Kh	0.1
Duration of injection, days	3 days
Amount H_2 Injected, kg	2,000 kg
Interval of injection, ft	15 ft
Location of injection	bottom
Depth, ft	1,550-1,600 ft
Thickness, ft	50 ft
Numerical model grid	210x216x50

discretization	
Residual saturation	0.2
SNR	Free of noise

Table 3. Summary of each simulation case.

Cases	Conditions
Case 1	Hydrogen injection at the bottom of the reservoir (Table 2)
Case 2	Same as Case 1 but with different realizations of permeability
Case 3	Same as Case 1 but maximum residual gas saturation of 0.06, compared to original 0.2
Case 4	Hydrogen injection at the middle of the reservoir
Case 5	Same as Case 1 but with different SNR

Case 1: Injection of hydrogen at the bottom of the reservoir

Case 1 focuses on the influence of injection of H_2 at the bottom of the reservoir. Figure 12 shows the simulated hydrogen saturation for the baseline, injection after 100 days and 365 days. Comparing the saturation models, we find that the saturation of the hydrogen plume will decrease from 70% to 40% and with time, the hydrogen plume will migrate upward and the shape of the plume will change. The source wavelet used in convolutional model for surface seismic is a 60 Hz Ricker wavelet. A bright spot appears in the poststack seismic responses, which can indicate the shape of the hydrogen plume. We also extract one trace in the middle of the plume (e.g., white dot line in Figure 12) to generate prestack AVA responses. Figure 13 displays the prestack AVA

responses of baseline, after 100 days, and after 365 days. Compared to the baseline, we find that the injected hydrogen can lead to small reflectivity series within the hydrogen plume. Additionally, it is obvious that with the increasing time, the amplitude of the extra small reflectivity increases. We experimented with what frequencies we could detect the H_2 plume in finer detail and found that we need at least 200 Hz for that, which is not feasible in the field settings.

ERT results are shown in Figure 14. We use an open-source Python-based ResIPy tool to conduct ERT modeling (Blanchy et al., 2020). For ERT experiments, the injection well is located in the middle of the hydrogen plume, and an observation well is located at distance of ~20 ft (~6 m) from the injection well. 50 electrodes are distributed from -490 m to -505 m with an interval of 0.3 m. For ERT inversion, we set value for tolerance to 1, the maximum number of iterations to 10, and smoothing factor to 50. The left panels shown in Figure 14 are the real resistivity model generated by Archie's law (Archie, 1942), which is commonly used to relate the resistivity of a porous medium to the saturation and resistivity of the pore fluid. In our experiments, we set formation water resistivity to 0.04 ohm.m, saturation exponent to 2, and cementation factor to 2, and tortuosity as 1. The right panels shown in Figure 14 are the zoomed inversion results. Compared to the real model, we can see that ERT is very sensitive to higher resistivity (e.g., marked by the black dot rectangles), which can effectively reveal the positions with higher saturation. However, it is noticeable that the ERT results after 365 days are not promising. The inverted result only shows positions with higher saturation at edge areas, and it is mainly caused by the fact that the thickness of the layers with higher resistivity is only about 0.3 m and the resolution of ERT cannot reach a good accuracy in the middle of the plume.

Figure 15 depicts the acoustic model-based crosshole seismic responses, the left panels are the velocity model, where the blue circles and triangles stand for the source and receiver positions.

We use a 1,000 Hz Ricker wavelet as the source and the source locations are marked by the black circles in Figure 15. Due to the crosshole seismic survey principles, we can see that the seismic responses are transmission dominated. From the baseline (Figure 15), we can see transmission and reflection waves from the bottom of the reservoir. It is evident that hydrogen plume can lead to a low-velocity area in the middle of the reservoir, and the plume will migrate horizontally over time. Multiple small events appear to be due to the transmission of the wave through the hydrogen plume. Figures 15a, b, c are the crosshole seismic responses of baseline, injection after 100 days, and injection after 365 days. Intuitively, there are apparent differences between the crosshole seismic responses of baseline and hydrogen injection. Nevertheless, the crosshole seismic difference between injection after 100 days and 365 days is slight.

Case 2: Injection at the bottom of the reservoir but with different realization of permeability

Case 2 aims to investigate the influence of permeability on time-lapse monitoring. The permeability model in case 2 conforms to Gaussian distribution with the same mean value of 50 md but different standard deviations from case 1. Like case 1, we can also estimate the corresponding poststack seismic responses by conducting rock physics modeling and convolving the reflectivity series with a 60 Hz source wavelet (Figure 16). Poststack seismic responses in Figures 16 show the formation of a bright spot after hydrogen injection. Figures 17 represents the prestack AVA responses corresponding to the locations. We find the injected hydrogen can cause more small reflectivity series within the plume over time. Figure 18 indicates that ERT is more sensitive to high resistivity and shows the positions with higher saturation within the hydrogen plume. Nevertheless, the decreasing hydrogen saturation leads to low resistivity, which makes it challenging to reveal the saturation distribution in the middle of the plume. Figure 19 represents the acoustic crosshole seismic responses of case 2. However, the crosshole seismic differences

are limited, indicating that crosshole seismic response is not sensitive to hydrogen plume when saturation ranges from 40% to 70%. Notably, permeability model is important for hydrogen storage.

Case 3: Injection at the bottom of the reservoir, with the effect of residual gas saturation

Case 3 mainly investigates the influence of residual gas saturation, which is the fraction of pore space in the reservoir that remains filled with hydrogen after another fluid has displaced hydrogen, typically brine. To elaborate, the parameter examined here is the maximum residual gas saturation, which is the increasing value of gas saturation due to hysteresis. Understanding how residual gas saturation affects hydrogen behavior is crucial for optimizing the performance of underground hydrogen storage systems. Compared to the baseline (case 1), the residual gas saturation in case 4 decreases to a maximum of 0.06. However, the poststack, prestack, ERT, and crosshole seismic responses of case 4 (Figures 20-23) are almost identical to case 1, which means that residual gas saturation has a small influence on geophysical responses. It is noticeable that residual gas saturation reduces the effective pore space available for hydrogen storage. Once hydrogen is injected into the reservoir, a portion of it may become trapped as residual gas, limiting the amount that can be recovered during withdrawal. Therefore, if we would like to design a cyclical hydrogen storage system, a low residual gas saturation helps to reduce the hydrogen loss.

Case 4: Injection in the middle of the reservoir

Case 4 shows the influence of the injection of H_2 in the middle of the reservoir. Using the same workflow as case 1, we generated poststack seismic responses of Case 4 as shown in Figure 24 also shows bright spot, which can describe the edge of the plume. Figure 25 shows the prestack AVA response of case 4, and we can see that the hydrogen plume results in strong reflection amplitude at the top interface of the reservoir as well as some interval small reflectivity series.

Figure 26 shows the resistivity model of baseline, injection after 100 days, and injection after 365 days as well as the corresponding ERT results, where we can see the hydrogen will concentrate under the caprock, causing high resistivity. As expected, ERT is more sensitive to high resistivity, enabling ERT to reveal the locations with higher hydrogen saturation (e.g., marked by the black dot rectangles). However, injection at the middle of the reservoir facilitates hydrogen to reach the confining layer, increasing the risk of hydrogen loss due to diffusion and geochemical interactions. Therefore, effective and real-time geophysical monitoring is required to better manage hydrogen storage if the injection is in the middle of the reservoir (in this case).

Figure 27 shows the crosshole seismic responses of Case 4, where we can see the velocity variation before and after hydrogen injection. We use a 1,000 Hz Ricker wavelet to generate crosshole seismic responses at the black circle. Notably, the difference between Figures 27d and 27f is too small to be distinguished, indicating that crosshole seismic survey is not sensitive to hydrogen plume variation when saturation ranges from 70% to 40%.

Case 5: Injection at the bottom of the reservoir, with varying SNR

Next, we discuss the noise effect on seismic responses from dynamic simulation-guided geophysical modeling results. To evaluate the noise level, we define signal to noise ratio (SNR) with the following form

$$SNR = 20log_{10}(\|\mathbf{S}_{clean}\|_2/\|N_{noi}\|_2), \tag{36}$$

where $\mathbf{S}_{clean}$ and $\mathbf{N}_{\mathrm{noi}}$ represent clean data and noise, respectively. Next, based on case 1, we add noise into the poststack, prestack, and crosshole seismic responses, and the results are displayed in Figures 28-30. For each situation, we keep the noise level unchanged during post-injection monitoring after 100 days and 365 days. However, due to the energy variation of original clean seismic responses, the calculated SNRs after 100 days and 365 days are not the same. As for

poststack data, we can see that although the bright spot is still visible with the increasing noise level, the data quality decreases, and the seismic responses corresponding to the top hydrogen plume are blurred, making it more challenging to distinguish the top boundary of hydrogen plume. Regarding prestack seismic, when SNR is about 5 dB (e.g., Figures 29a and 29c), the quality of prestack data is acceptable. However, when SNR decreases to about -5 dB (e.g., Figures 29b and 29d), the continuity of event will be deteriorated, and some useful signals will be masked by the noise. Figure 30 depicts the noisy crosshole seismic responses after 100 days and 365 days. Similar to prestack data, when SNR equals to about 5 dB, we can see transmission wave and reflection wave from the bottom reservoir (Figure 30). Nevertheless, with the increasing noise level, it is obvious that noise can degrade the quality of crosshole seismic data, leading to weak signals and potential misinterpretations. In view of this, we suggest multiple noise tests in the field to ensure high repeatability and denoising to improve data quality to increasing the fidelity of time-lapse data to accurately track hydrogen plume.

Table 4: NRMS comparison between different cases.

NRMS	Poststack seismic	ERT	Crosshole seismic
Case 1	166.4% (100 days) 145.7% (365 days)	55.67% (100 days) 46.05% (365 days)	167.7% (100 days) 166.8% (365 days)
Case 2	163.7% (100 days) 149.2% (365 days)	64.33% (100 days) 56.03% (365 days)	167.9% (100 days) 167.6% (365 days)
Case 3	172.3% (100 days) 163.6% (365 days)	60.34% (100 days) 48.73% (365 days)	166.9% (100 days) 168% (100 days)
Case 4	185% (100 days)	60.73% (100 days)	168.6% (100 days)

	178.7% (365 days)	55.89% (365 days)	169.2% (365 days)

Table 5: NRMS comparison under different SNRs.

NRMS	Poststack seismic	Prestack seismic	Crosshole seismic
100 days	185.5% (3.4 dB) 189.7% (-6.6 dB)	199.81% (5.4 dB) 199.83% (-4.6 dB)	186.9% (5.4 dB) 189.4% (-1.6 dB)
365 days	185.4% (3.1 dB) 189.6% (-6.8 dB)	199.82% (4.8 dB) 199.83% (-5.1 dB)	186.4% (5 dB) 189.2% (-2 dB)

According to our experiments, injection of H_2 at either the bottom or middle of the reservoir have their pros and cons. Injection at the middle of the reservoir facilitates hydrogen to reach the confining layer, increasing the leakage risk (e.g., fractures in confining rock, diffusion, among others). The injection of H_2 at the bottom of the reservoir seems suited for reservoirs with good vertical permeability. Hydrogen injected at the bottom naturally rises due to buoyancy, ensuring that it fills the entire vertical extent of the reservoir. More importantly, injection near the bottom of the reservoir helps to keep hydrogen away from the confining rock, reducing the risk of leakage. Another advantage is that injecting at the bottom of the reservoir (in this case) allows only the fluid effects to be discerned from the geophysical data, as opposed to the injection at the middle of the reservoir, leading H_2 to migrate towards the confining rock and resulting in geophysical anomalies resulting from both lithology and fluid contrasts. The migration toward the confining rock is more controlled due to internal reservoir complexities, giving operators more time to monitor hydrogen movement and avoid leakage. However, injecting at the bottom of the reservoir is not efficient for eventual production of hydrogen.

Permeability distribution in the reservoir can lead to varying plume distribution, which would impact geophysical responses. In reservoirs with high permeability, hydrogen can be injected more easily, resulting in rapid saturation of the storage formation. Low-permeability formations, on the other hand, may require higher injection pressures to achieve the same storage volumes, leading to operational challenges, affecting geophysical data.

CONCLUSIONS

We build a rock physics framework for determining the elastic properties of hydrogen-saturated rock, which can impact monitoring design. We model the variation of elastic properties as a function of lithology, porosity, hydrogen saturation, and patchiness exponent, and diffusion. AVA responses are mainly concentrated in class III and it will vary from class III to class II over time, indicating more hydrogen loss.

We tested a workflow integrating geology and dynamic reservoir simulation to predict geophysical responses of surface seismic, ERT, and crosshole seismic. Our study shows the complex and variable geophysical responses corresponding to different geologic (permeability and residual gas saturation) and operational (injection position: bottom and middle of the reservoir and SNR) controls directing the patterns of H_2 movement in the reservoir over time.

For a small volume of hydrogen injection in a reservoir with a small thickness, surface seismic with a conventional dominant frequency of 60 Hz is unsuitable for monitoring. Both seismic and ERT present their challenges and benefits regarding resolution, sensitivity to H_2 saturation, sensor geometries, and well casing type. It is noticeable that ERT can indicate the position of the hydrogen plume with higher saturation, which may help to determine the distribution of hydrogen. The NRMS differences of ERT, compared to surface seismic and crosshole seismic are more intuitive,

indicating that ERT is more sensitive to hydrogen plume in the subsurface. Beyond various geologic controls, SNR in the field settings will essentially control repeatability and what can be accurately interpreted from 4D geophysical data.

NOMENCLATURE AND ACRONYMS

ERT: electrical resistivity tomography

SNR: signal to noise ratio

FWI: full waveform inversion

DL: deep learning

VRH: Voigt-Reuss Hill

H-S: Hashin–Strikman

AVA: amplitude versus angle

ACKNOWLEDGEMENT

The authors would like to thank GeoH$_2$ Industrial Affiliates Program and Bureau of Economic Geology at the University of Texas at Austin for funding. Authors thank Dr. Mark Shuster for reviewing the article. Thanks to the developers of ResIPy and Madagascar tools used in this study.

REFERENCES

Abdellatif, M., M. Hashemi, and S. Azizmohammadi, 2023, Large-scale underground hydrogen storage: integrated modeling of reservoir-wellbore system, International Journal of Hydrogen Energy, 48, no.50, 19160–19171.

Archie, G. E., 1942, The electrical resistivity log as an aid in determining some reservoir characteristics, Transactions of the AIME, 146, 54-62.

Bhattacharya, S., Swaminadhan, S., Bakhshian, S., 2024, Building Realistic Time-Lapse Seismic Models for CO2 Plume Monitoring, Integrating Geology, Reservoir Simulation, and Rock Physics: Case Study from an Onshore CCS Site, presented at SEG Geophysical Research for Gigatonnes CO2 Storage, Golden

Blanchy, G., Saneiyan, S., Boyd, J., McLachlan, P., and Binley, A., 2020, ResIPy, an intuitive open source software for complex geoelectrical inversion/modeling, Computers & Geosciences, 137,104423.

Borello, E. S. et al., 2024, Underground Hydrogen Storage Safety: Experimental Study of Hydrogen Diffusion through Caprocks, Energies, 17, no.2, 394.

Brie, A., F. Pampuri, A. Marsala, and O. Meazza, 1995, Shear sonic interpretation in gas-bearing sands: SPE Annual Technical Conference, 30595, 701–710.

Chabab, S., P. Théveneau, C. Coquelet, J. Corvisier, and P. Paricaud, 2020, Measurements and predictive models of high-pressure H2 solubility in brine (H2O+NaCl) for underground hydrogen storage application, International Journal of Hydrogen Energy, 45, no.56, 32206–33220.

Castagna, J., H. Swan, and D. Foster, 1998, Framework for AVO gradient and intercept interpretation, Geophysics, 63, no. 3, 948–956.

Fuad M. I. Ahmad, H. Zhao, M. S. Jaya, and E. A. J. Jones, 2023, Rock Physics Modeling of Hydrogen-bearing Sandstone: Implications for Natural Hydrogen Exploration and Storage, SPE Annual Technical Conference and Exhibition, SPE-214789-MS.

Fomel, S., P. Sava, I. Vlad, Y. Liu, and V. Bashkardin, 2013, Madagascar: open-source software project for multidimensional data analysis and reproducible computational experiments, Journal of Open Research Software, 1:e8, DOI: http://dx.doi.org/10.5334/jors.ag

Gao, K., N. M. Creasy, L. Huang, and M. R. Gross, 2024, Underground hydrogen storage leakage detection and characterization based on machine learning of sparse seismic data, International Journal of Hydrogen Energy, 61, 137–161.

Gassmann, F., 1961, Uber die Elastizitat poroser Medien, 96, 1–23.

Heinemann, N. et al., 2021, Enabling large-scale hydrogen storage in porous media – the scientific challenges, Energy & Environmental Science, 14, 853–864.

Hill, R., 1952, The elastic behaviour of a crystalline aggregate, Proceesing of the Physical Society, 65, no. 5, 349–354.

Hashin, Z., and S. Shtrikman, 1963, A variational approach to the theory of the elastic behaviour of multiphase materials, Journal of the Mechanics and Physics of Solids, 11, no. 2, 127–140.

Li, C., and Bhattacharya, S., 2024, Seismic amplitude variation with angle response of hydrogen-saturated rock: Implications on subsurface monitoring, presented at AAPG-SEG IMAGE conference, Houston.

Mindlin, R. F., 1949, Compliance of elastic bodies in contact: Journal of Applied Mechanics, 16, no. 3, 259–268.

Machado, M. V. B., M. M. Alhotan, G. R. Jerauld, M. Delshad, and K. Sepehrnoori, 2024, Fluid Property Characterization for Underground Gas Storage, Journal of Clean Energy and Energy

Storage, 1, 2450004 (24 pages).

Pfeiffer, W., S. Hagrey, D. Köhn, W. Rabbel, and S. Bauer, 2016, Porous media hydrogen storage at a synthetic, heterogeneous field site: numerical simulation of storage operation and geophysical monitoring, Environmental Earth Sciences, 75, Art no. 1177.

Robinson, E. A., 1967, Predictive decomposition of time series with application to seismic exploration, Geophysics, 32, 418-484.

Shuey, R. T., 1985, A simplification of the zoeppritz equations, Geophyiscs, 50, no. 4, 609–614.

Shuster, M., Bhattacharya, S., Duncan, I., Eichhubl, P., Hosseini, S., Javadpour, F., Kipper J., Lin, N., Nicot, J.P., and Ren, B., 2021, Hydrogen infrastructure expansion requires realistic framework, Oil & Gas Journal, pages 1-9.

Strauch, B., Pilz, P., Johannes Hierold, J., and Zimmer, M., 2023, Experimental simulations of hydrogen migration through potential storage rocks, International Journal of Hydrogen Energy, Volume 48, Issue 66, Pages 25808-25820.

Yang, J., X. He, S. Wang, and H. Chen, 2024, Monitoring underground hydrogen storage migration and distribution using time-lapse acoustic waveform inversion, International Journal of Hydrogen Energy, 69, 272-281.

Zeng, L., A. Keshavarz, Q. Xie, and S. Iglauer, 2022, Hydrogen storage in Majiagou carbonate reservoir in China: geochemical modelling on carbonate dissolution and hydrogen loss, International Journal of Hydrogen Energy, 47, no.59, 24861–24870.

Zivar, D., S. Kumar, and J. Foroozesh, 2021, Underground hydrogen storage: A comprehensive review, International Journal of Hydrogen Energy, 46, no. 45, 23436–23462.

Zhang M., and Y. Li, 2024, The role of geophysics in geologic hydrogen resources, Journal of Geophysics and Engineering, 21, no.4, 1242–1253.

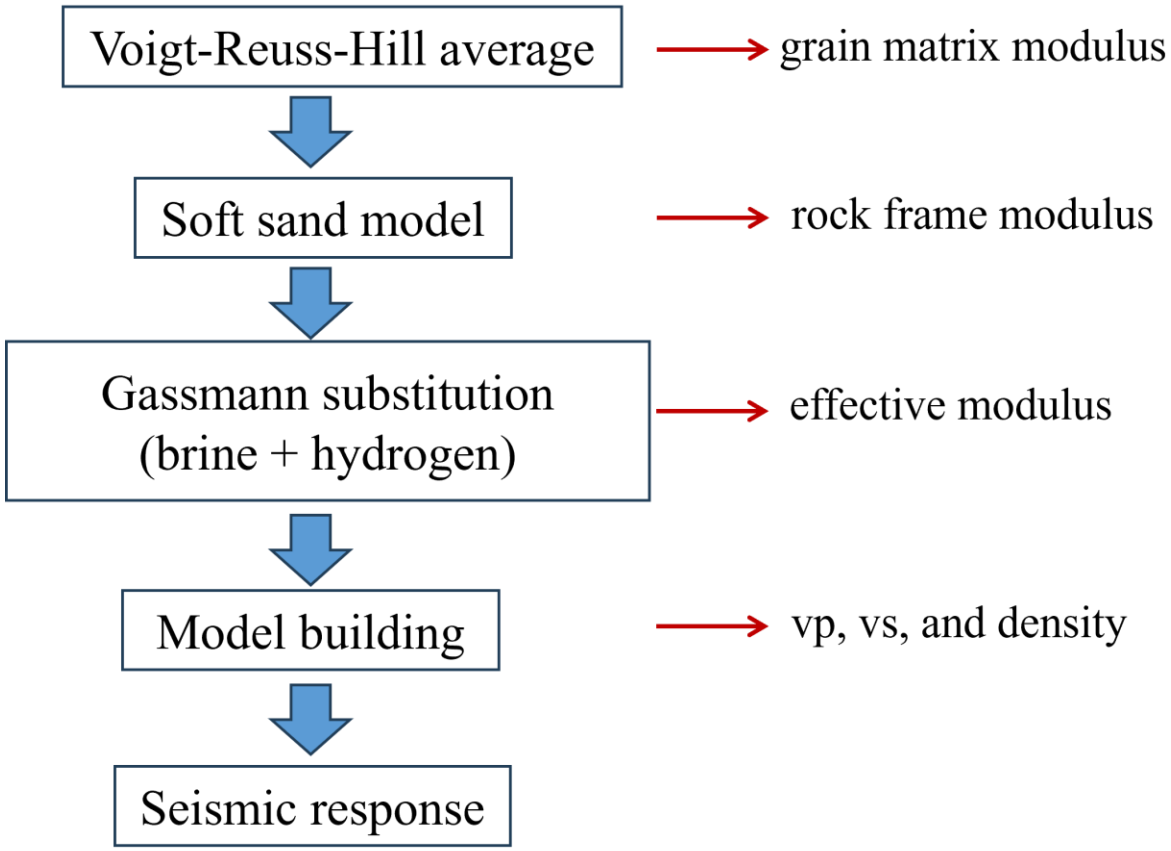

Figure 1. The workflow of rock physics modeling.

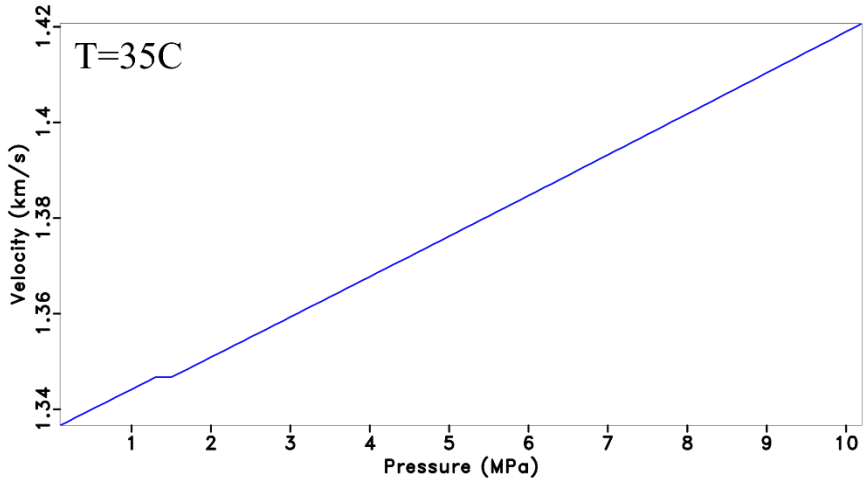

(a)

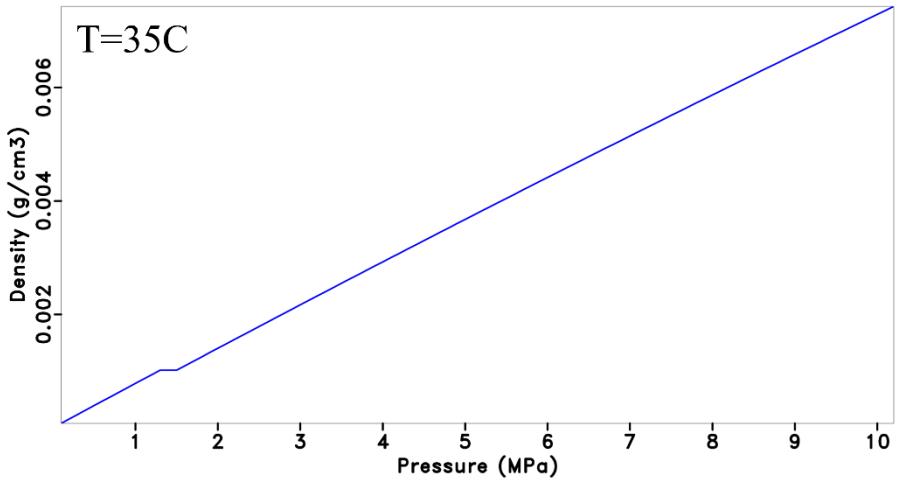

(b)

Figure 2. Hydrogen properties vs. pressure at 35 C. (a) Velocity. (b) Density.

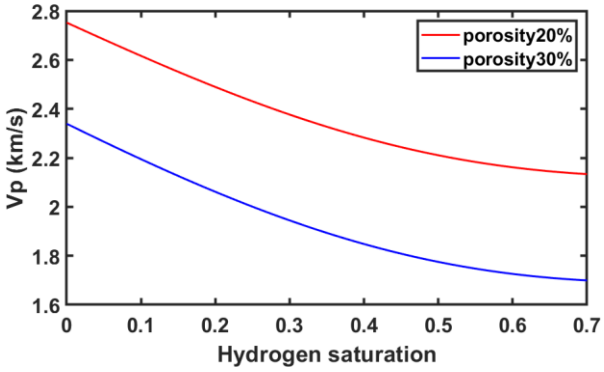

(a)

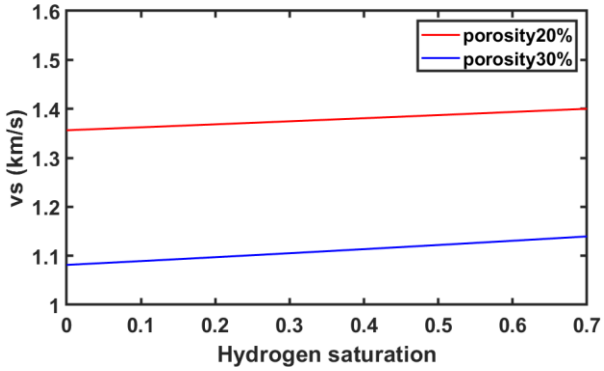

(b)

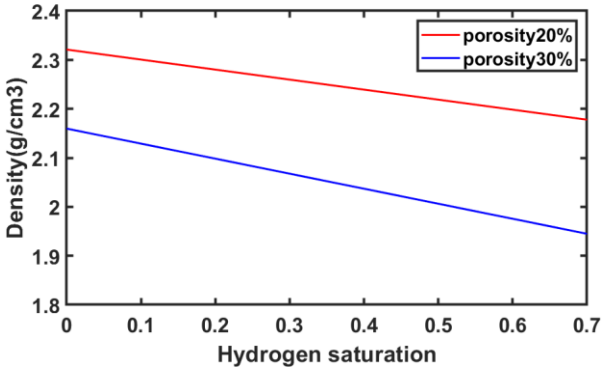

(c)

Figure 3. (a) Vp variation of hydrogen under different hydrogen saturation and porosity. (b) Vs variation of hydrogen under different hydrogen saturation and porosity. (c) hydrogen density variation under different hydrogen saturation and porosity (modified after Li and Bhattacharya,

2024).

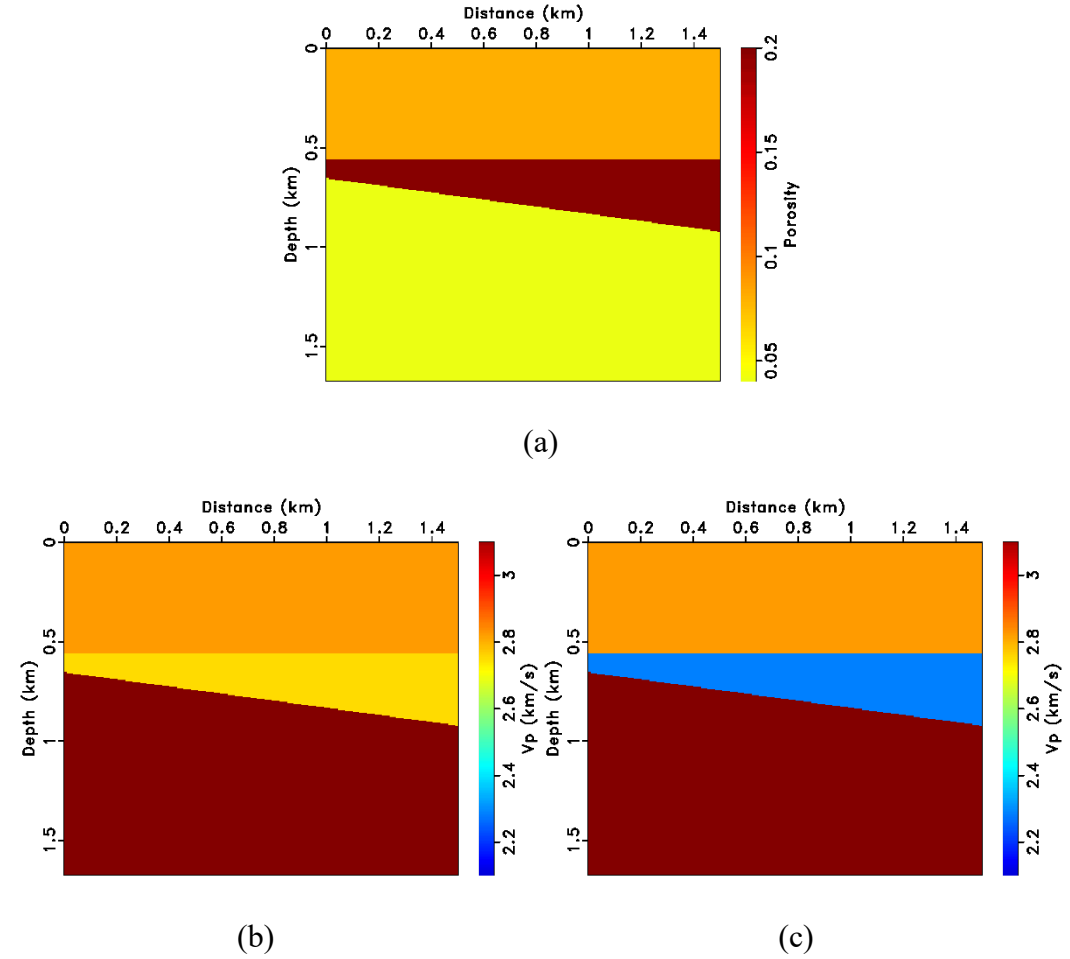

Figure 4. (a) Porosity model. (b) Vp before hydrogen injection. (c) Vp after hydrogen injection stops.

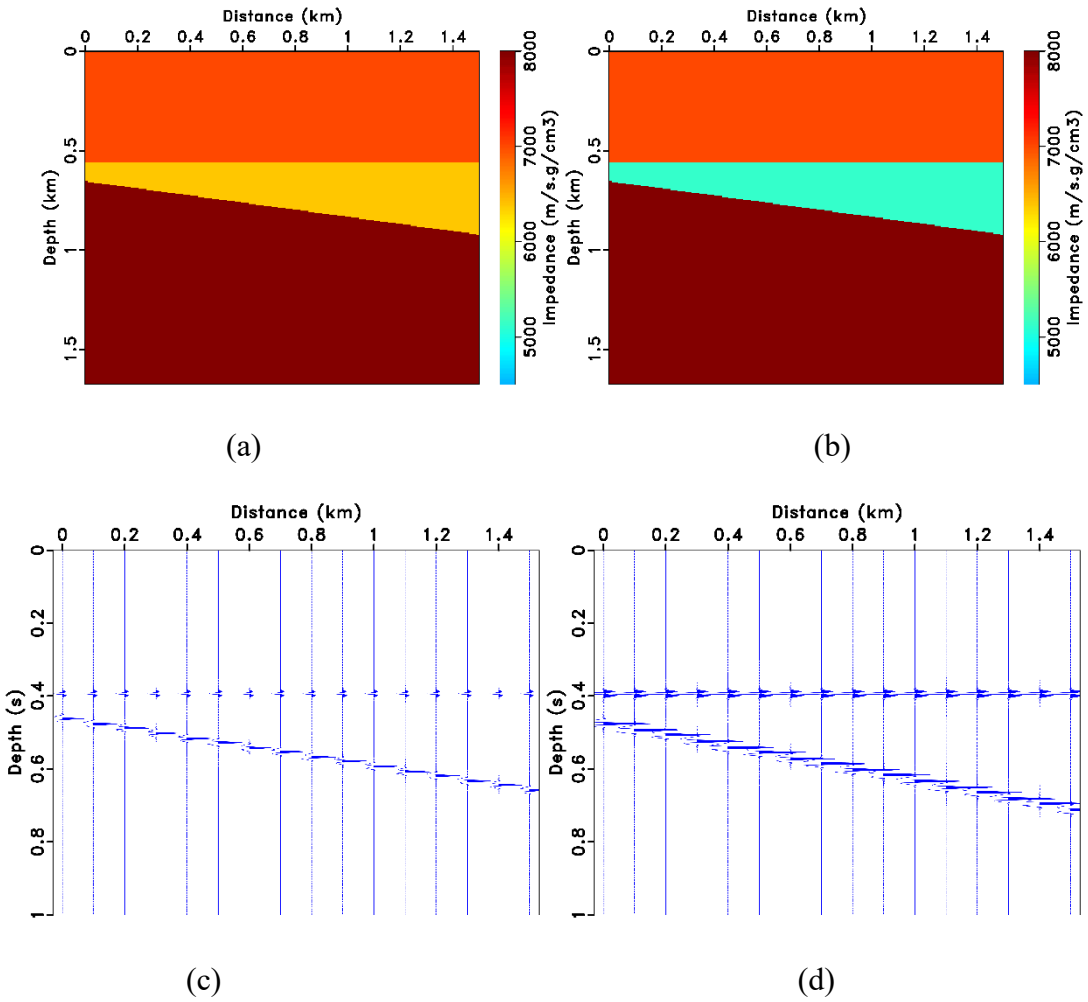

Figure 5. (a) Impedance before hydrogen injection. (b) Impedance after hydrogen injection. (c) Poststack seismic response before hydrogen injection. (d) Poststack seismic response after hydrogen injection stops.

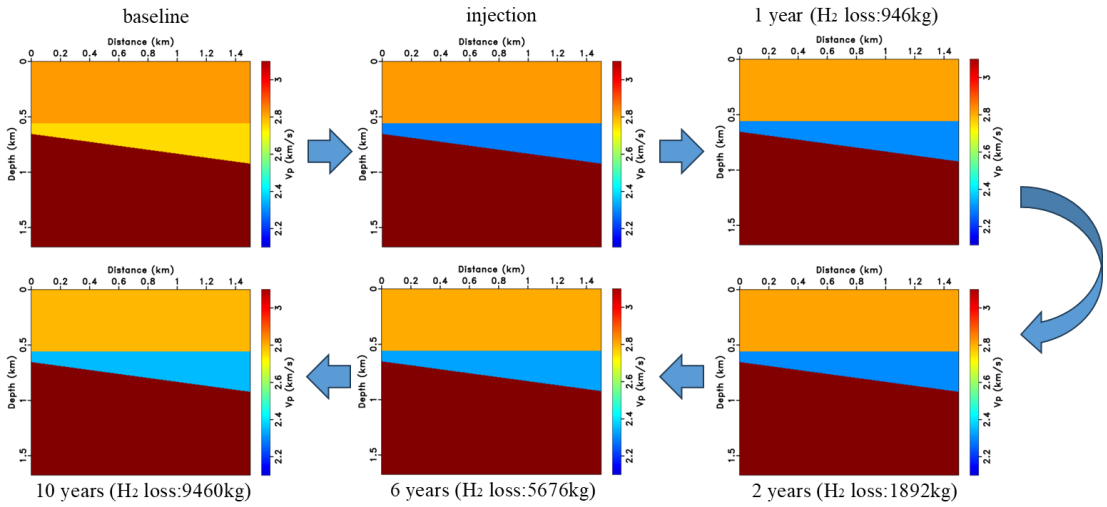

Figure 6. Velocity variation caused by diffusion effects after injection stops. The effect of diffusion on velocity is very small.

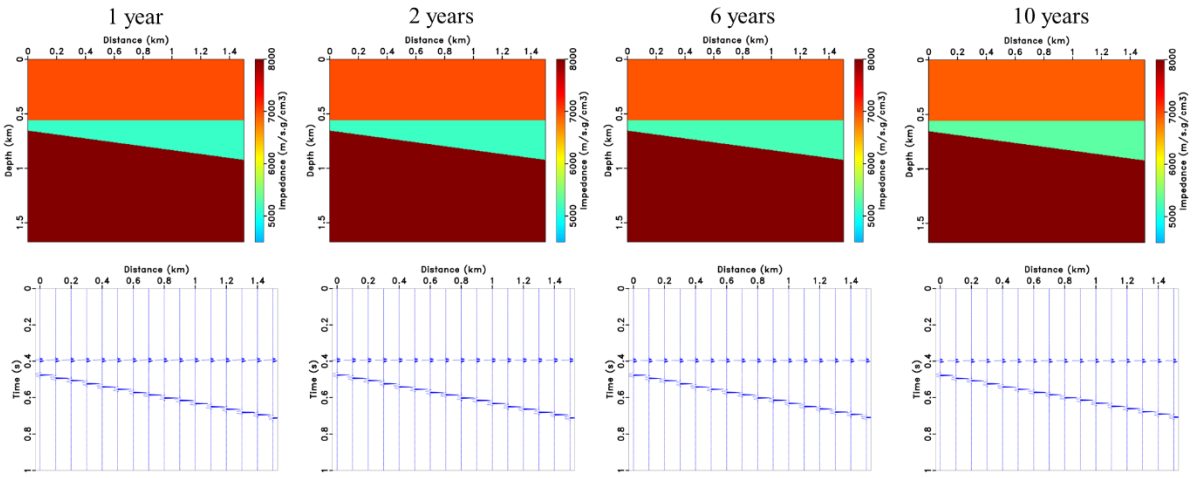

Figure 7. Poststack seismic responses influenced by diffusion effect after injection stops. The effect of diffusion is very small.

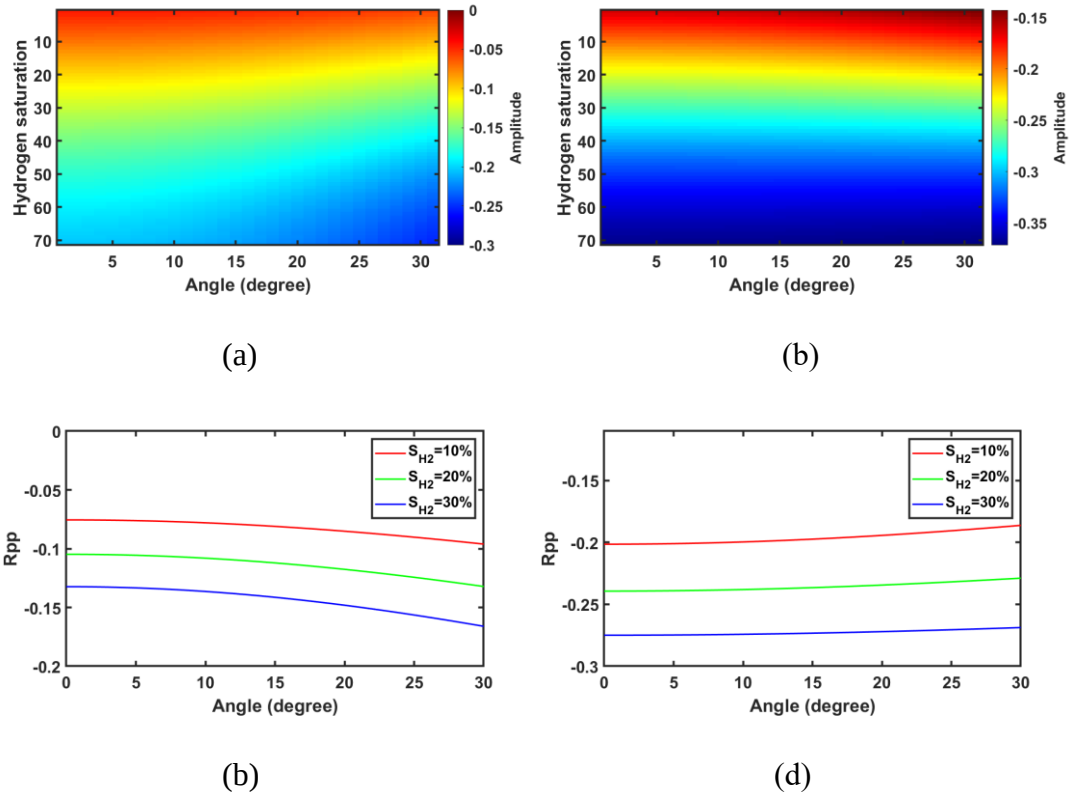

Figure 8. (a) Prestack AVA responses under different hydrogen saturations when $\phi = 20\%$ (b) Prestack AVA responses under different hydrogen saturations when $\phi = 30\%$. (c) Extracted single trace from Figure 8a. (d) Extracted single trace from Figure 8b.

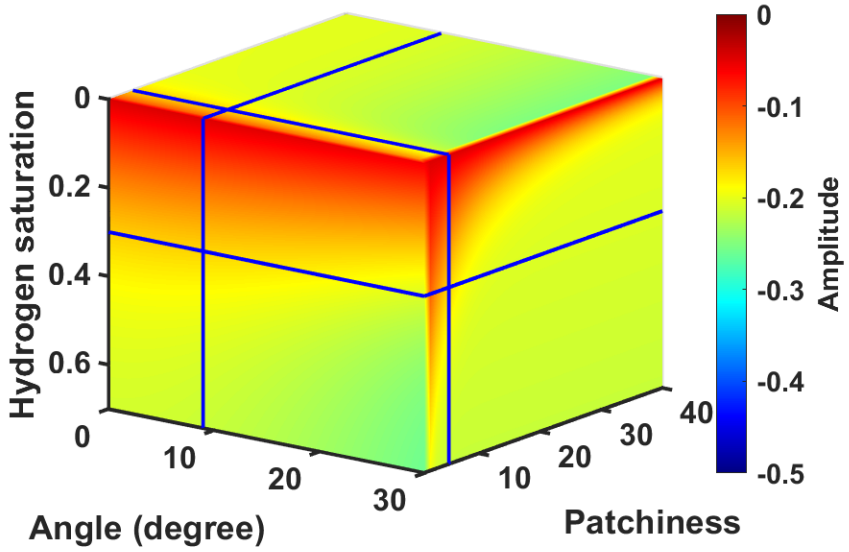

Figure 9. Prestack reflectivity variation with different hydrogen saturations and patchiness (modified after Li and Bhattacharya, 2024).

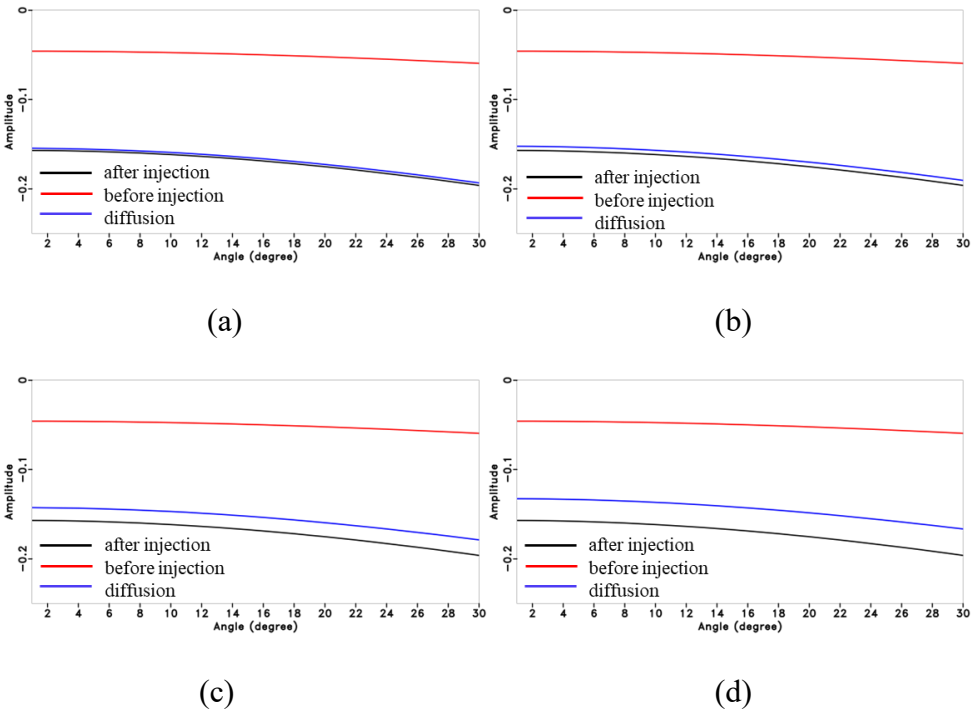

Figure 10. The effect of diffusion on prestack AVA after (a) one year, (b) two years, (c) six years, and (d) 10 years.

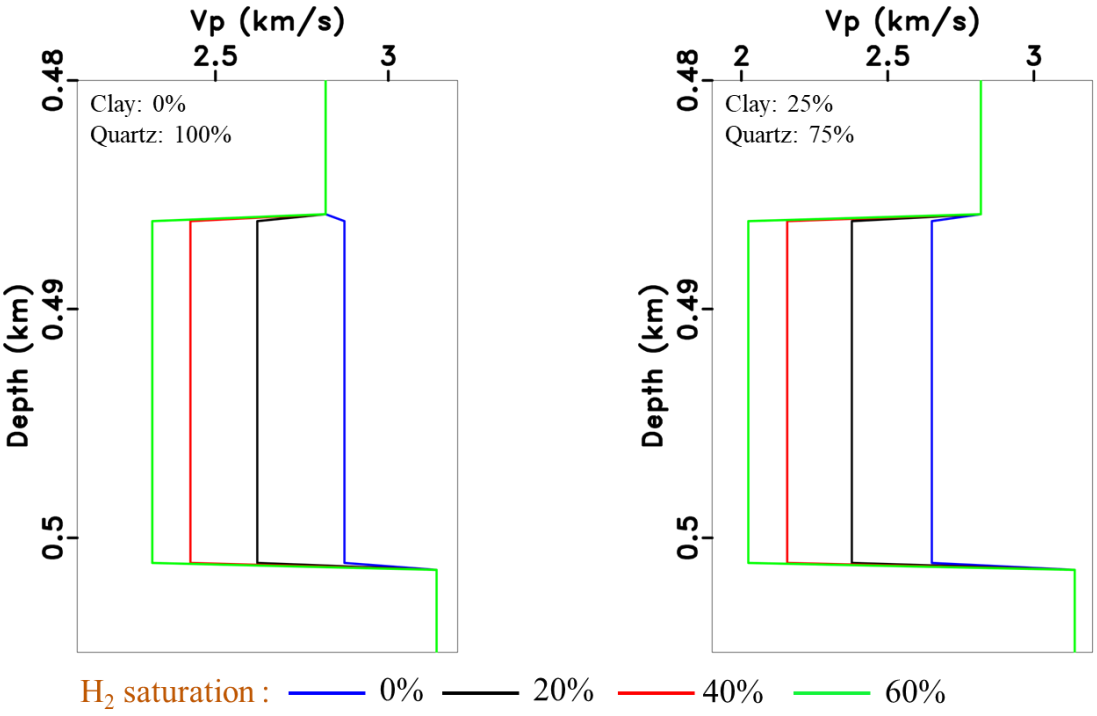

Figure 11. Influence of clay fraction on velocity variation under different hydrogen saturations.

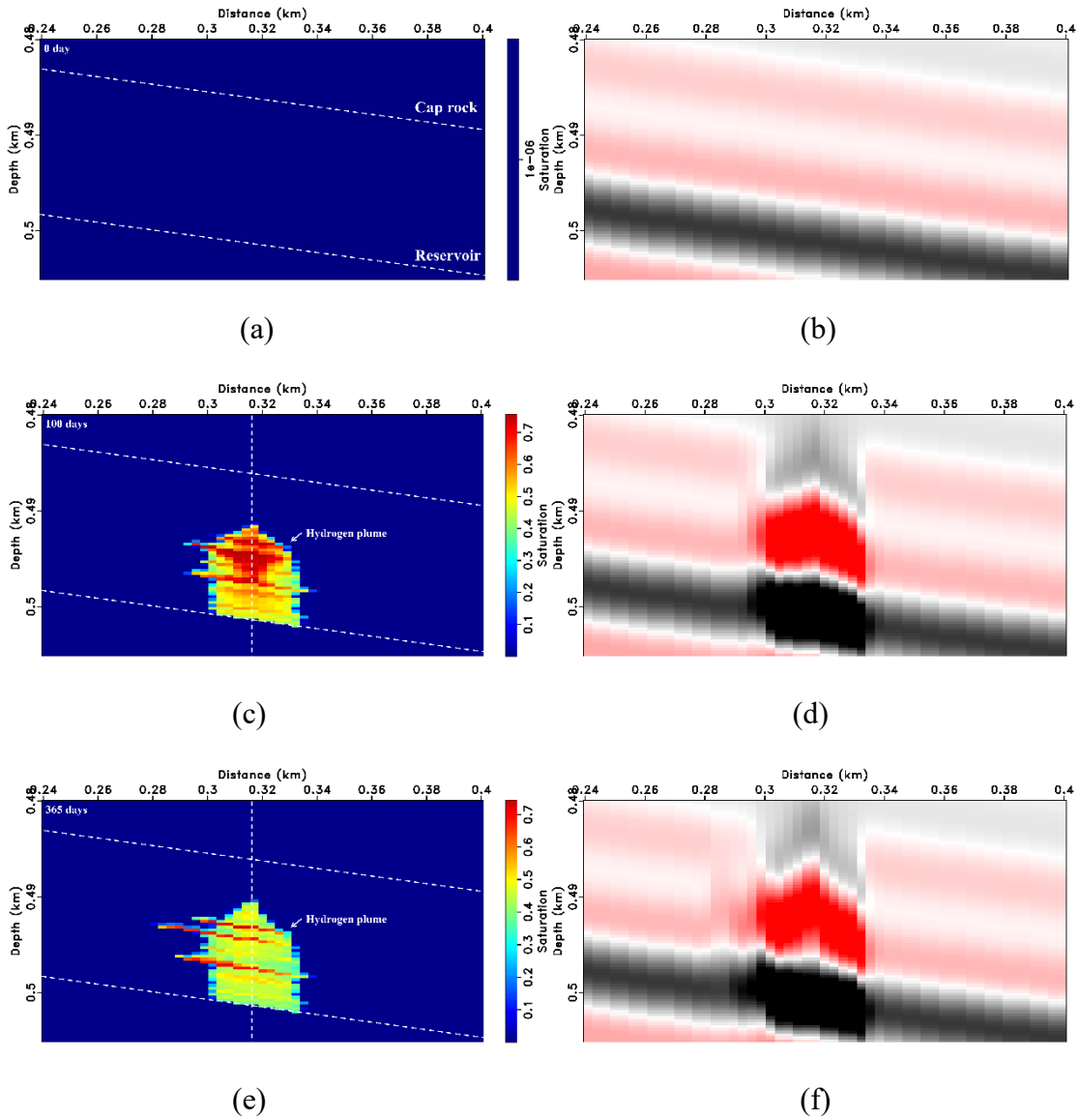

Figure 12. (a) Baseline saturation model. (b) Poststack seismic response corresponding to baseline. (c) Saturation model of hydrogen injection after 100 days (case 1). (d) Poststack seismic response corresponding to Figure 12c. (e) Saturation model of hydrogen injection after 365 days (case 1). (f) Poststack seismic response corresponding to Figure 12e.

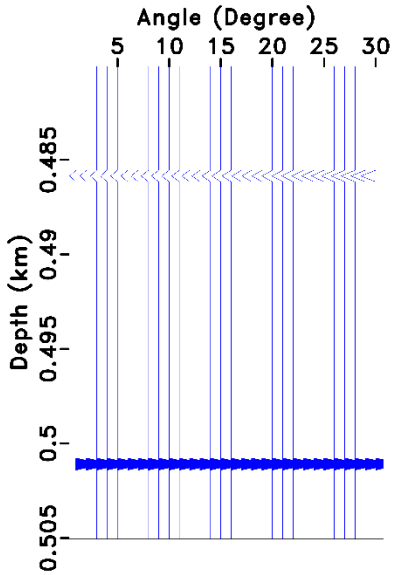

(a)

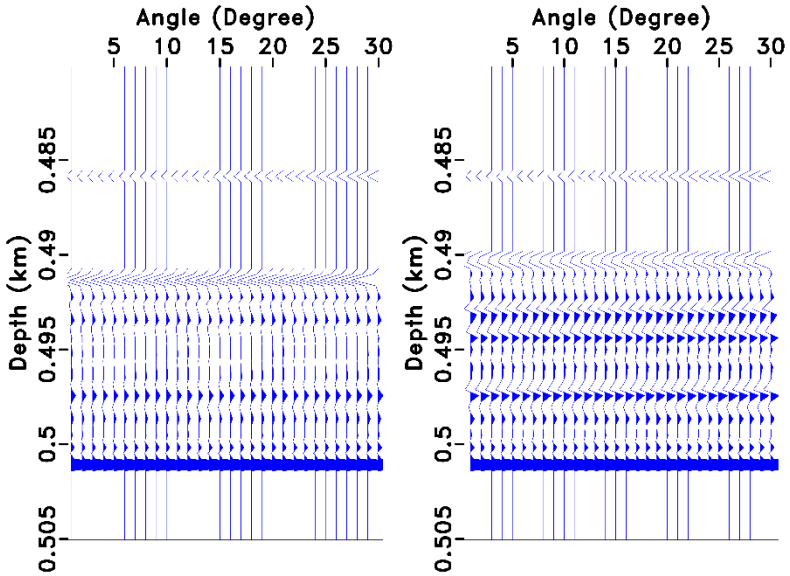

(b) (c)

Figure 13. Prestack angle-gather at the injection well location for (a) baseline, (b) after 100 days (case 1), and (c) after 365 days (case 1).

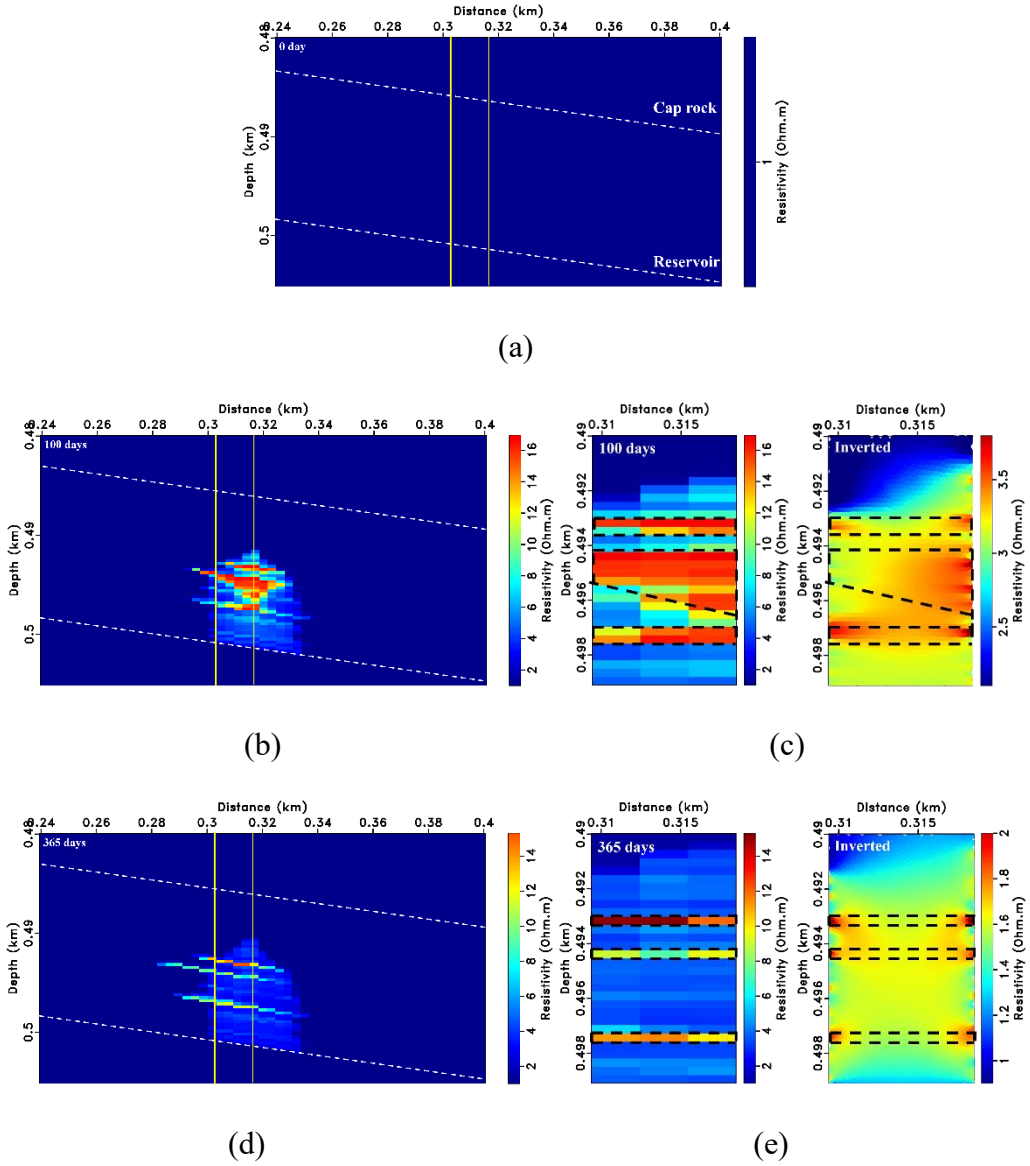

Figure 14. (a) Baseline resistivity model. (b) Resistivity model of hydrogen injection after 100 days (case 1). (c) Zoomed ERT inversion result after 100 days (case 1). (d) Resistivity model of hydrogen injection after 365 days (case 1). (e) Zoomed ERT inversion result after 365 days (case 1).

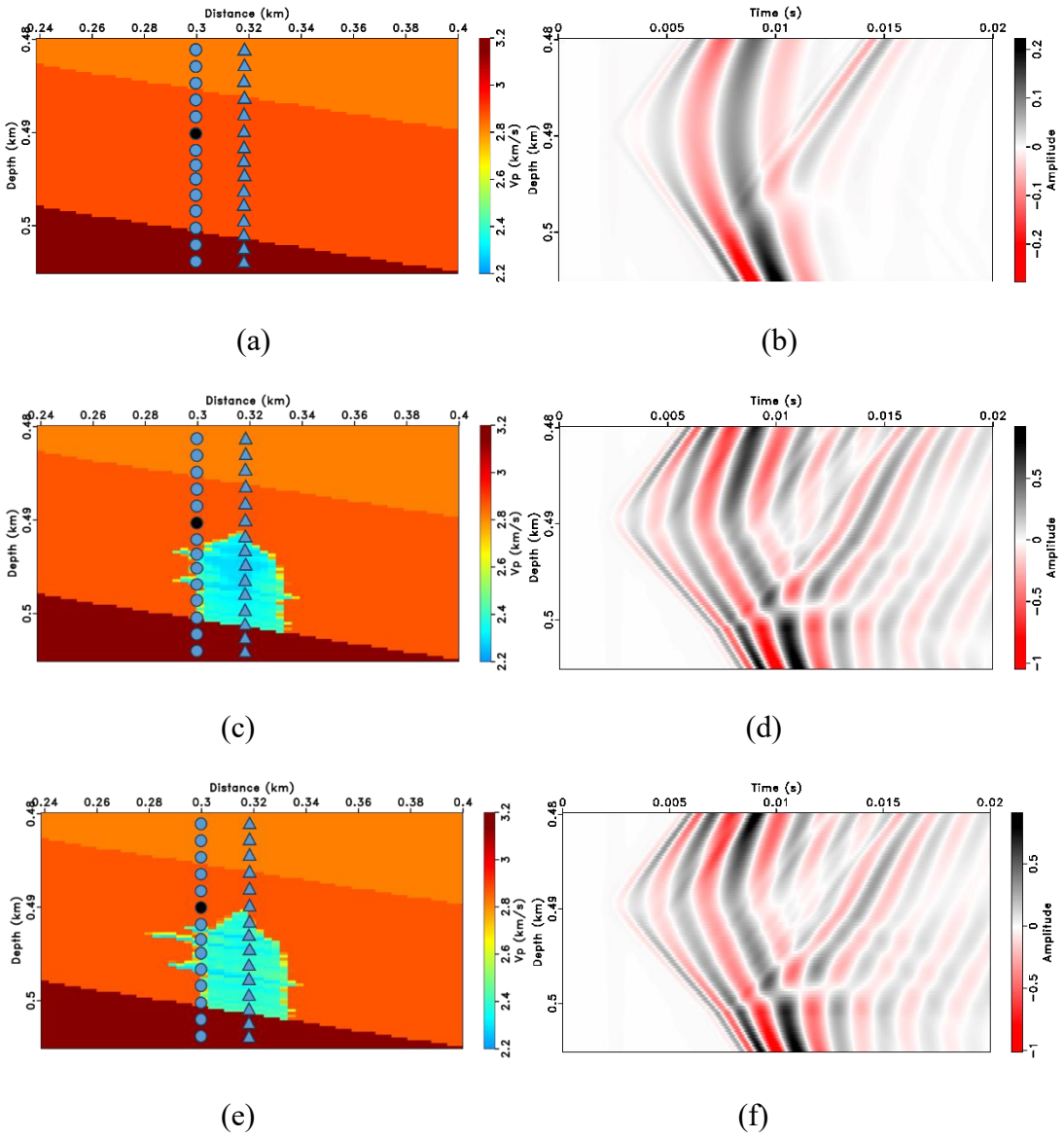

Figure 15. (a) 2D slice of baseline velocity model. (b) Crosshole seismic response corresponding to Figure 15a. (c) 2D slice of velocity model after 100 days (case 1). (d) Crosshole seismic response corresponding to Figure 15c. (e) 2D slice of velocity model after 365 days (case 1). (f) Crosshole seismic response corresponding to Figure 15e.

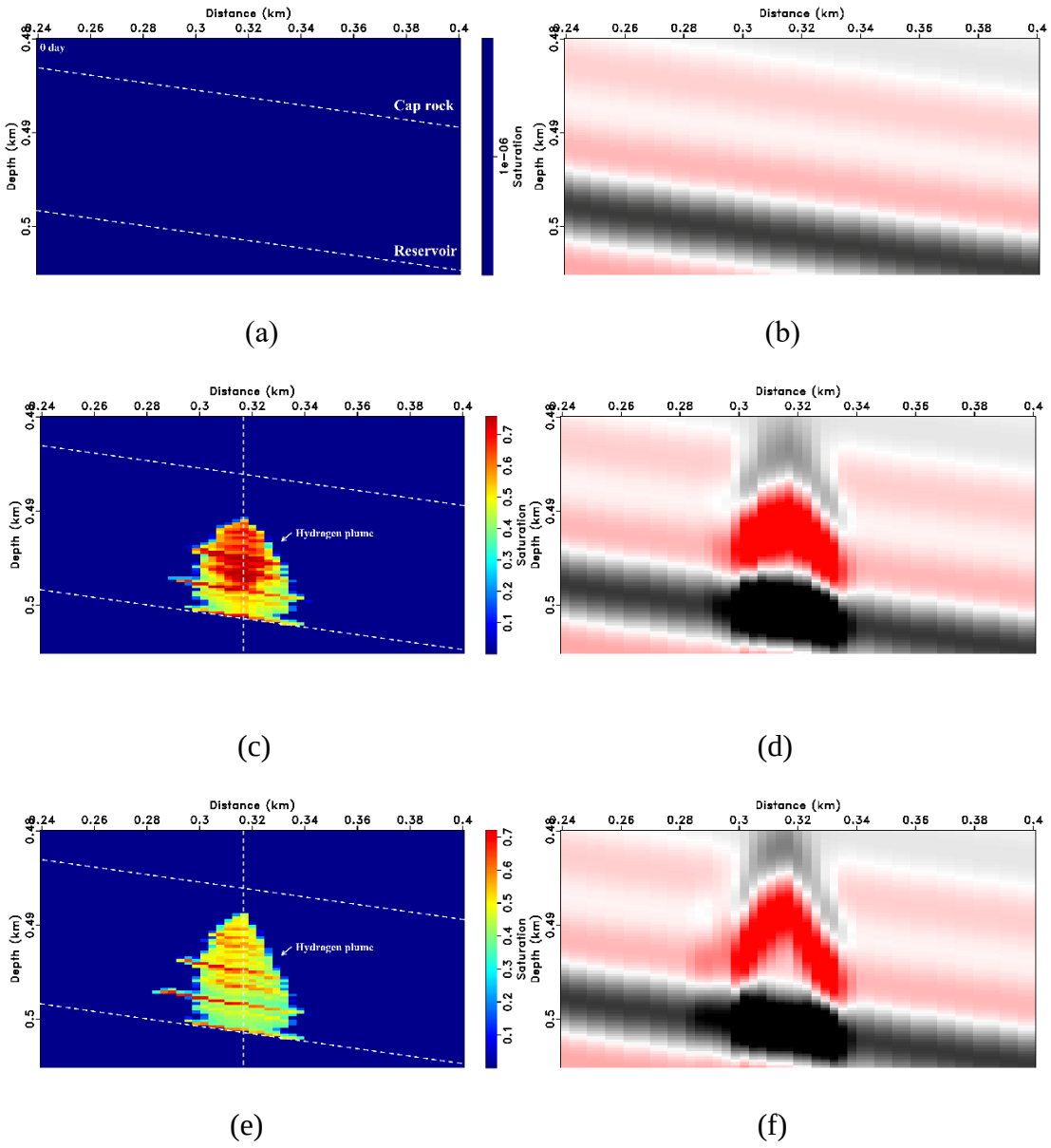

Figure 16. (a) Baseline saturation model. (b) Poststack seismic response corresponding to baseline. (c) Saturation model of hydrogen injection after 100 days (case 2). (d) Poststack seismic response corresponding to Figure 16c. (e) Saturation model of hydrogen injection after 365 days (case 2). (f) Poststack seismic response corresponding to Figure 16e.

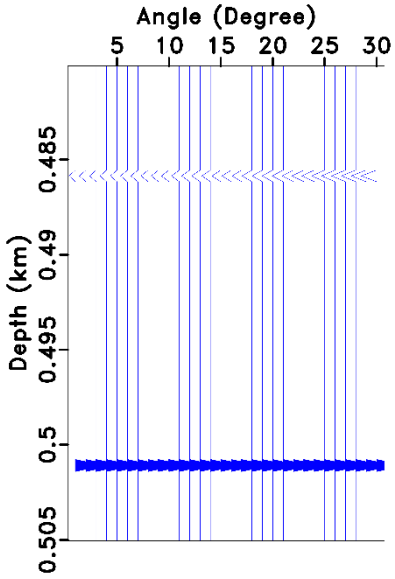

(a)

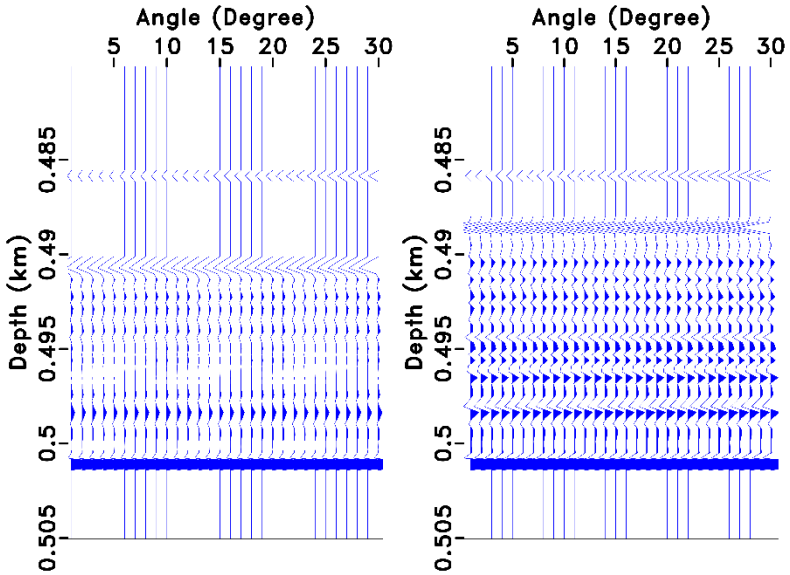

(b) (c)

Figure 17. Prestack angle-gather at the injection well location (a) baseline, (b) after 100 days (case 2), and (c) after 365 days (case 2).

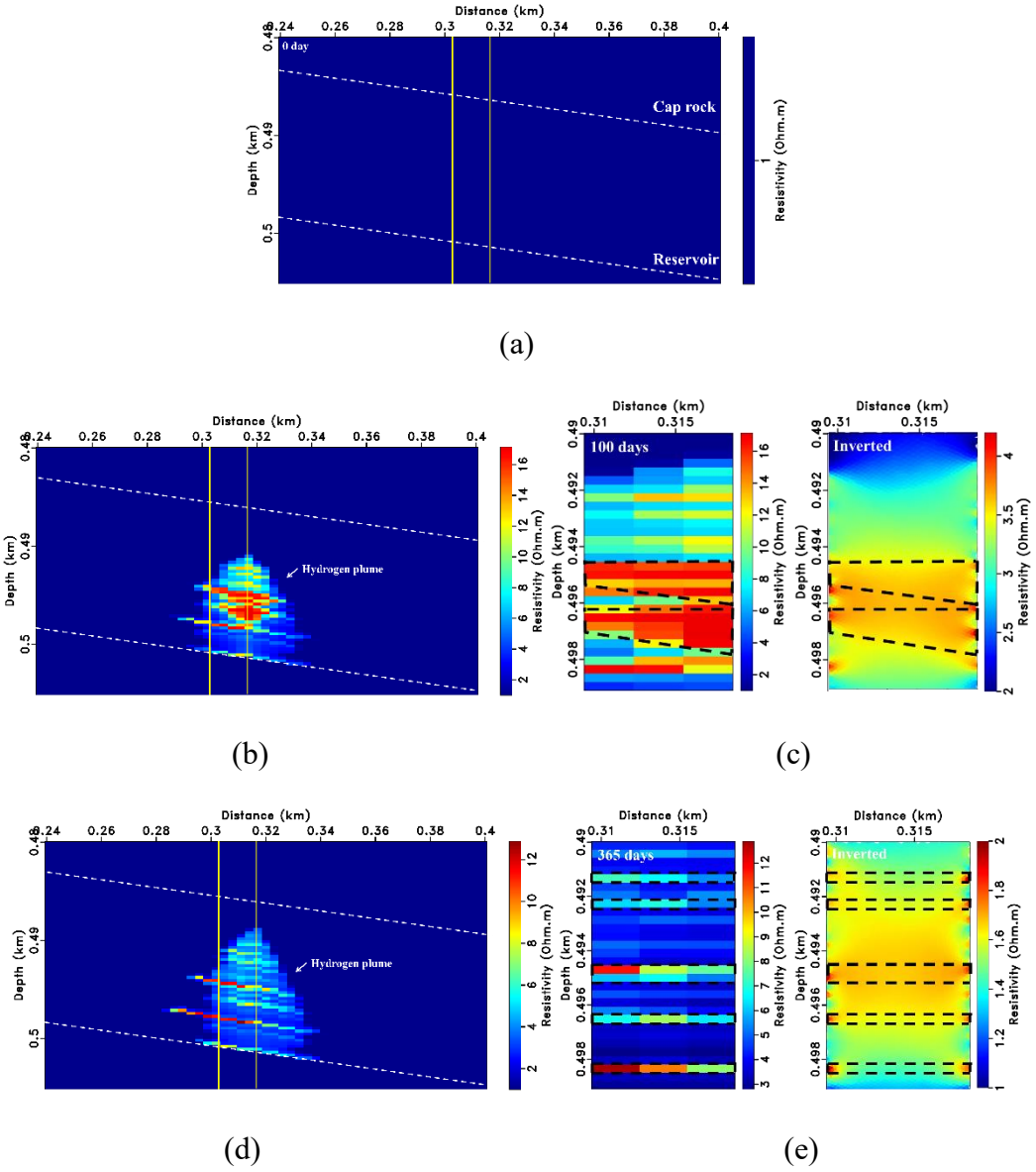

Figure 18. (a) Baseline resistivity model. (b) Resistivity model of hydrogen injection after 100 days (case 2). (c) Zoomed ERT inversion result after 100 days (case 2). (d) Resistivity model of hydrogen injection after 365 days (case 2). (e) Zoomed ERT inversion result after 365 days (case 2).

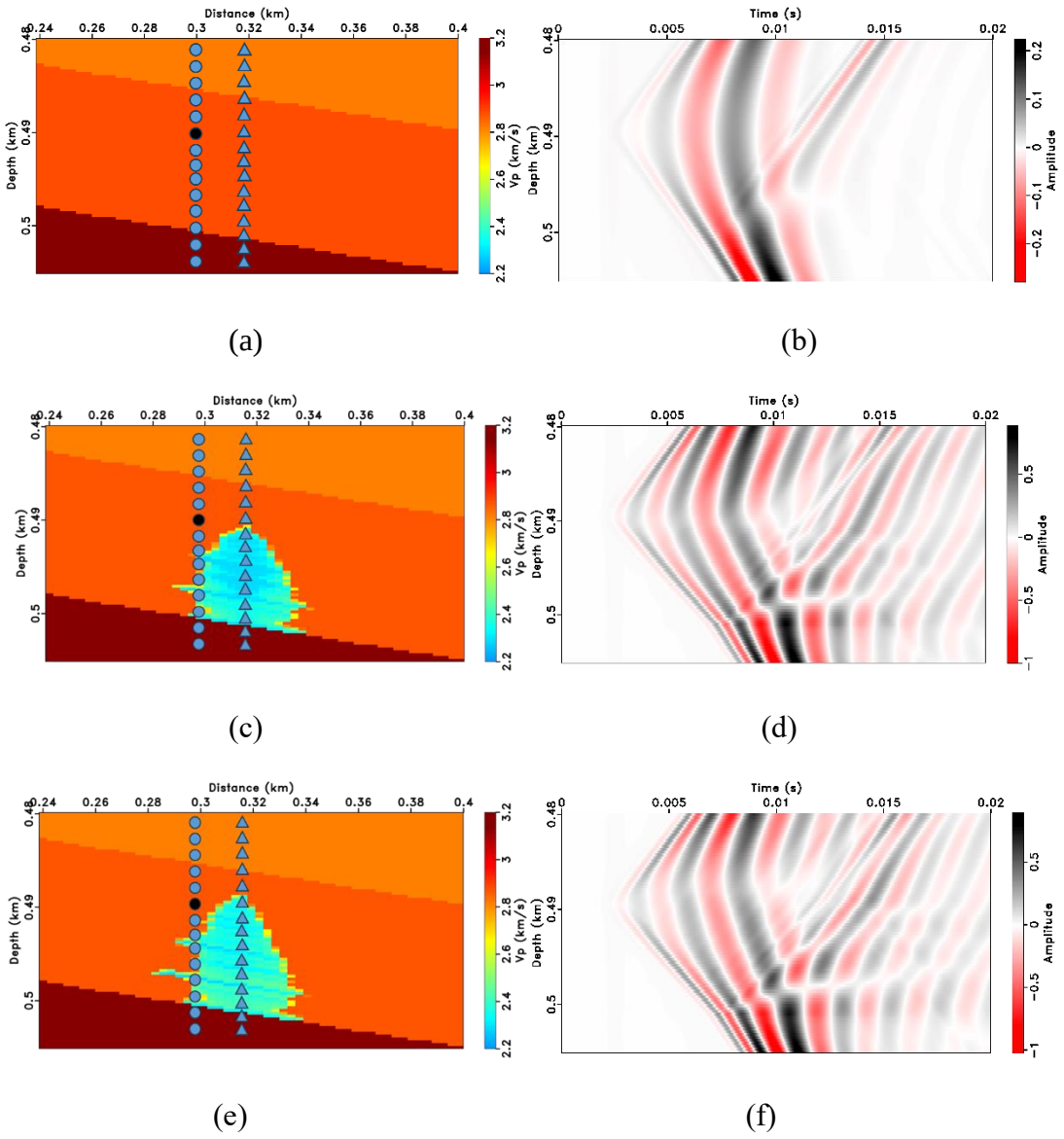

Figure 19. (a) 2D slice of baseline velocity model. (b) Crosshole seismic response corresponding to Figure 19a. (c) 2D slice of velocity model after 100 days (case 2). (d) Crosshole seismic response corresponding to Figure 19c. (e) 2D slice of velocity model after 365 days (case 2). (f) Crosshole seismic response corresponding to Figure 19e.

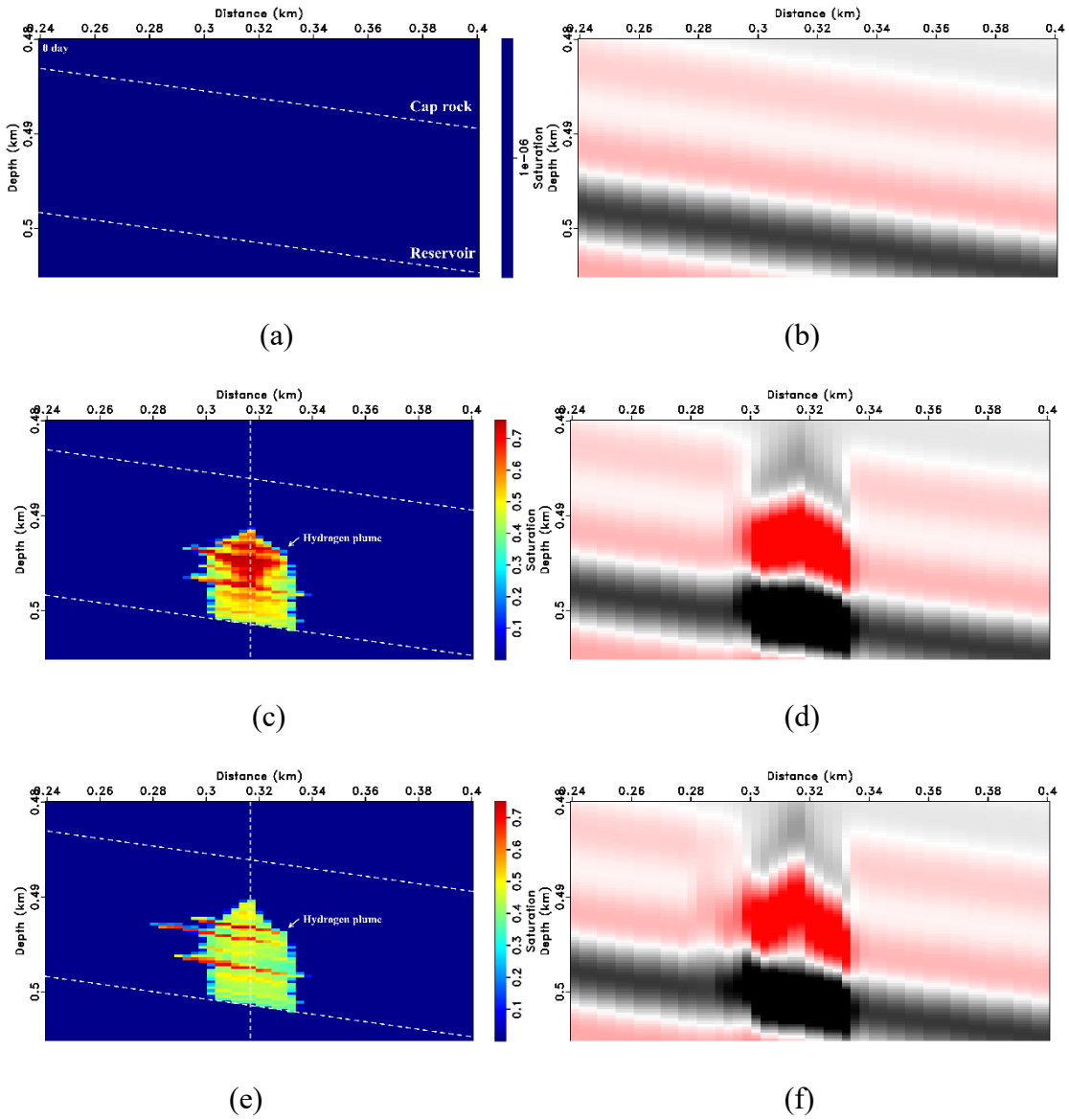

Figure 20. (a) Baseline saturation model. (b) Poststack seismic response corresponding to baseline. (c) Saturation model of hydrogen injection after 100 days (case 3). (d) Poststack seismic response corresponding to Figure 20c. (e) Saturation model of hydrogen injection after 365 days (case 3). (f) Poststack seismic response corresponding to Figure 20e.

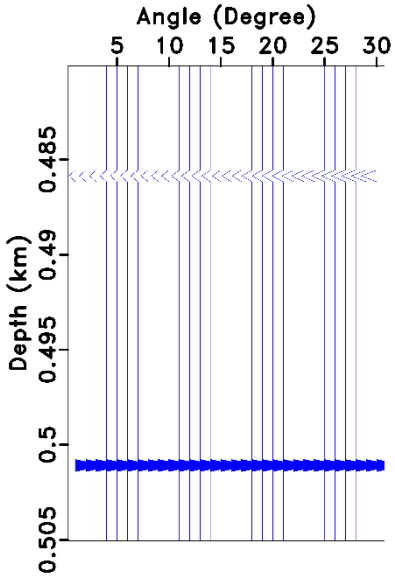

(a)

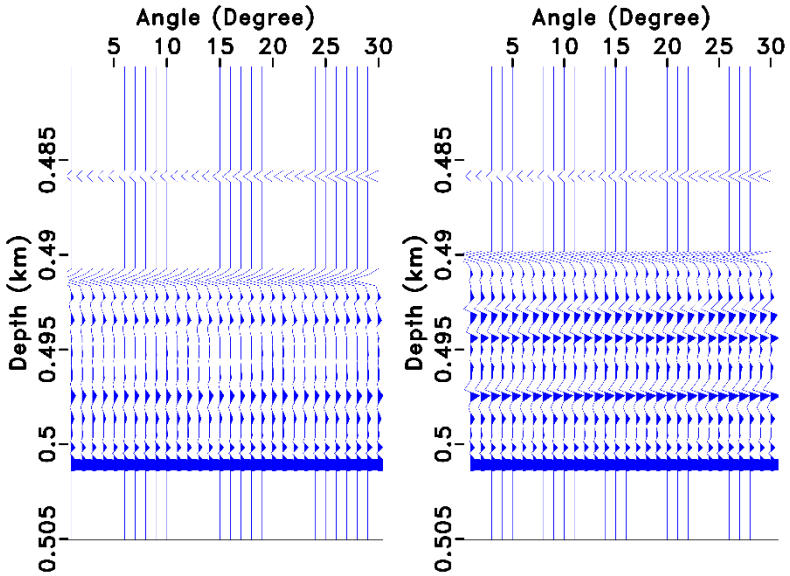

(b) (c)

Figure 21. Prestack angle-gather at the injection location (a) baseline, (b) after 100 days (case 3), and (c) after 365 days (case 3).

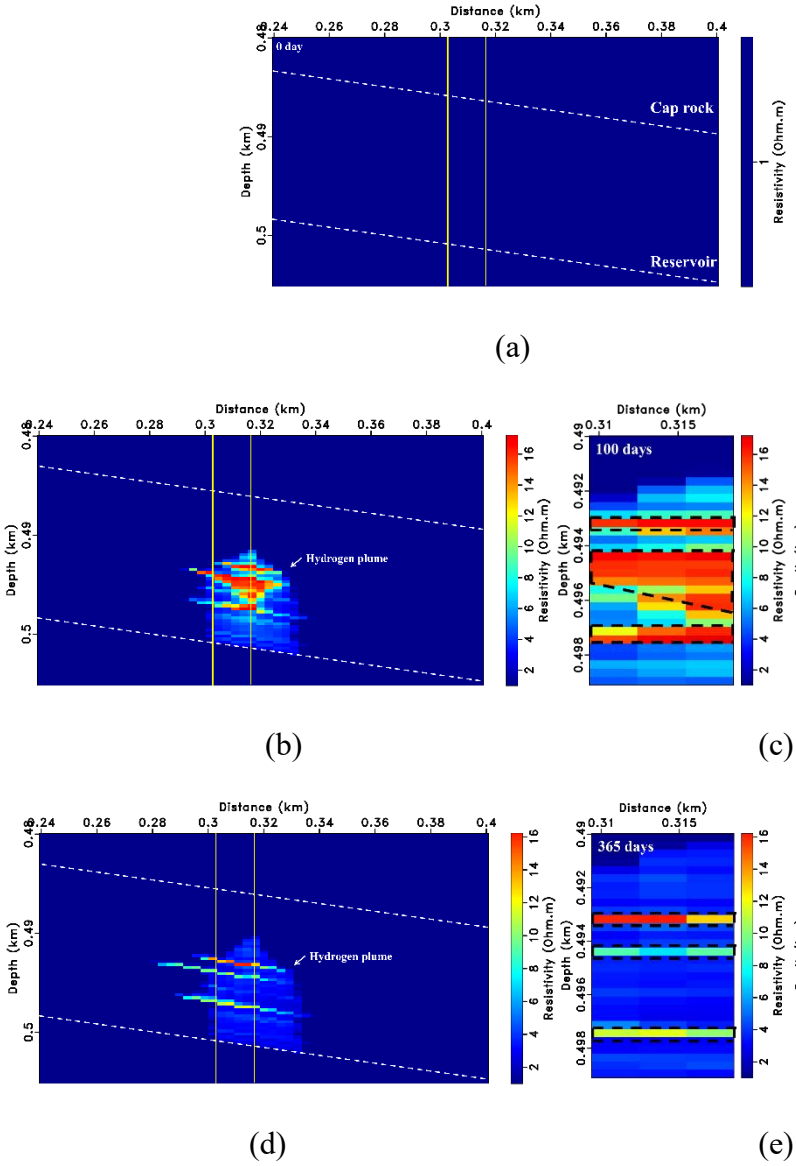

Figure 22. (a) Baseline resistivity model. (b) Resistivity model of hydrogen injection after 100 days (case 3). (c) Zoomed ERT inversion result after 100 days (case 3). (d) Resistivity model of hydrogen injection after 365 days (case 3). (e) Zoomed ERT inversion result after 365 days (case 3).

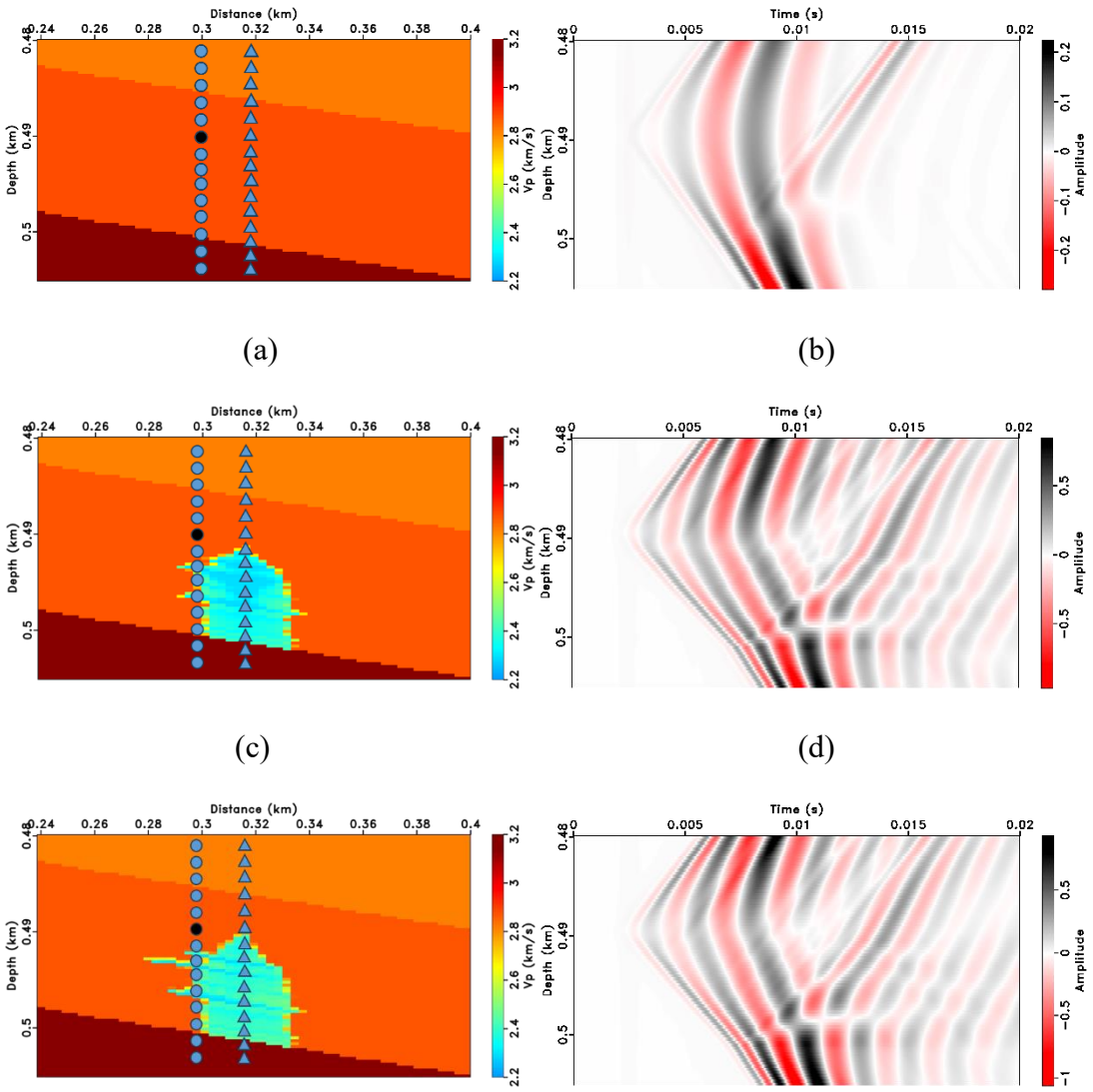

Figure 23. (a) 2D slice of baseline velocity model. (b) Crosshole seismic response corresponding to Figure 23a. (c) 2D slice of velocity model after 100 days (case 3). (d) Crosshole seismic response corresponding to Figure 23c. (e) 2D slice of velocity model after 365 days (case 3). (f) Crosshole seismic response corresponding to Figure 13e.

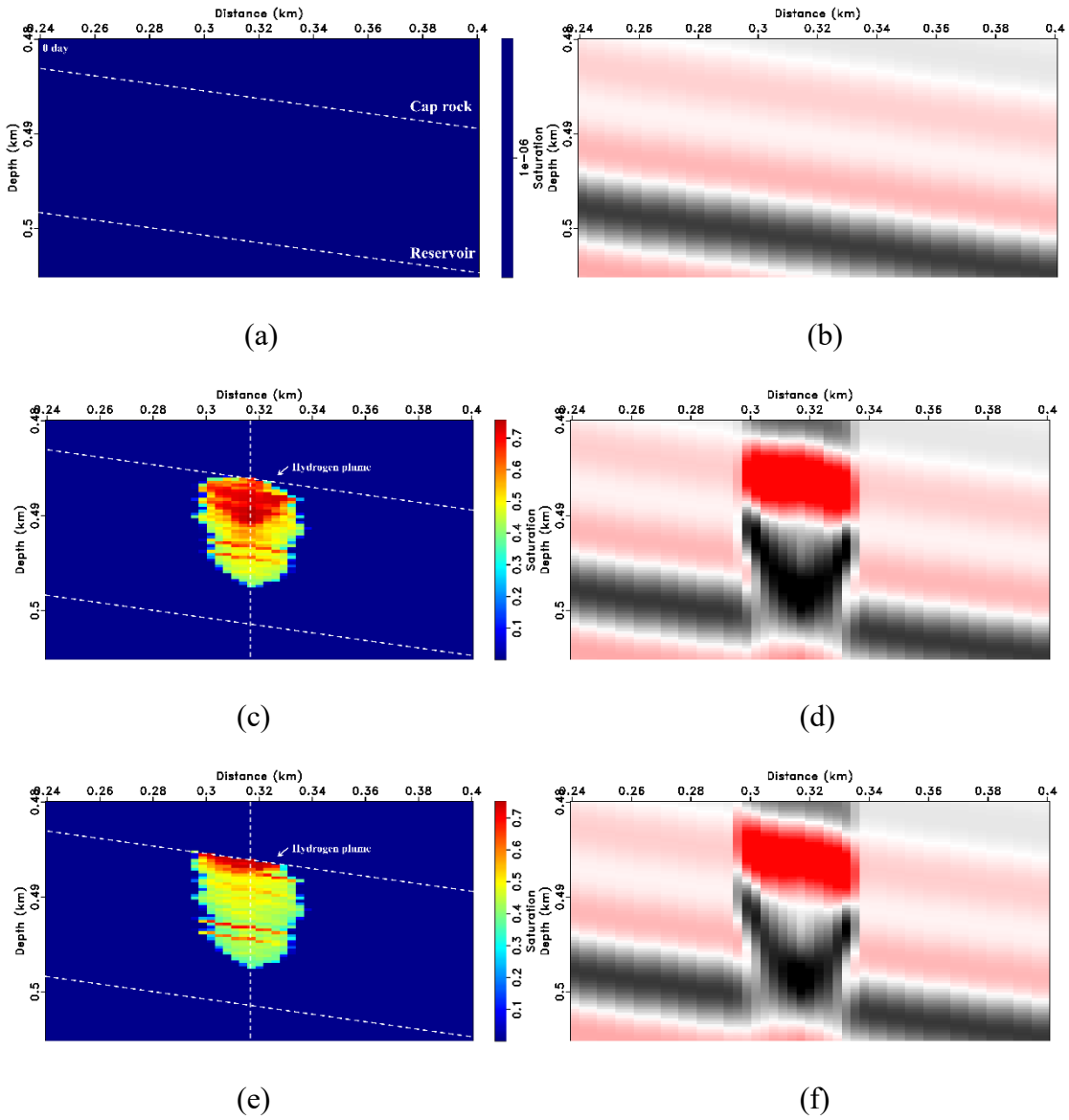

Figure 24. (a) Baseline saturation model. (b) Poststack seismic response corresponding to baseline. (c) Saturation model of hydrogen injection after 100 days (case 4). (d) Poststack seismic response corresponding to Figure 24c. (e) Saturation model of hydrogen injection after 365 days (case 4). (f) Poststack seismic response corresponding to Figure 24e.

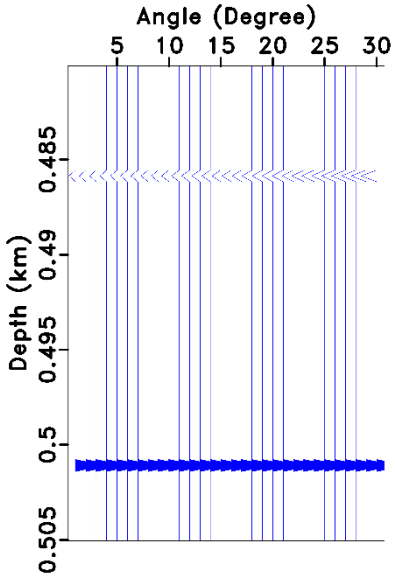

(a)

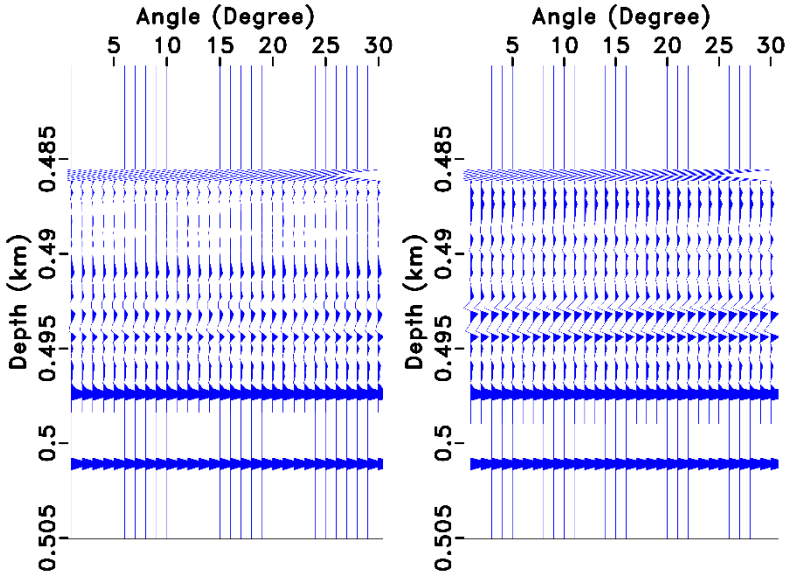

(b) (c)

Figure 25. Prestack angle-gather at the injection well location (a) baseline, (b) after 100 days (case 4), and (c) after 365 days (case 4).

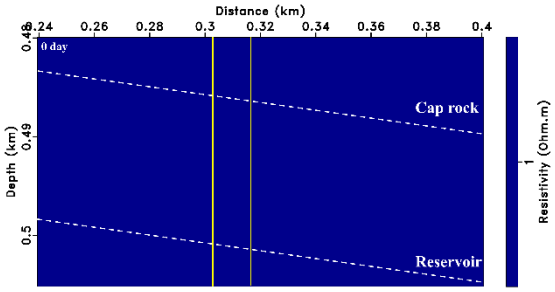

(a)

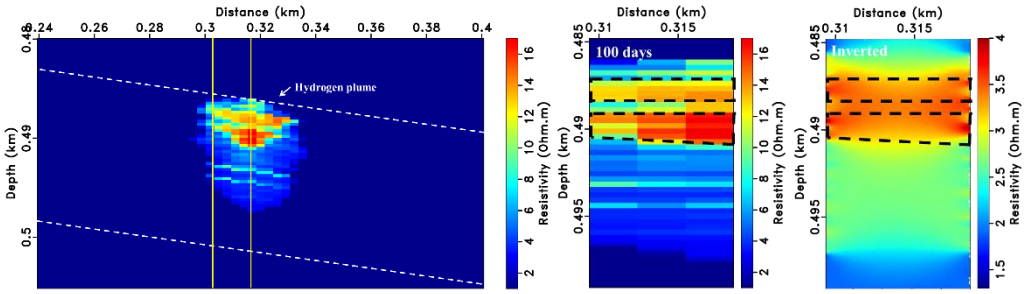

(b) (c)

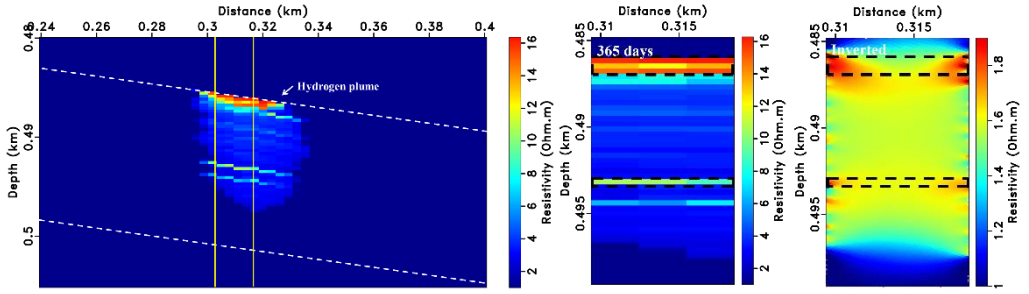

(d) (e)

Figure 26. (a) Baseline resistivity model. (b) Resistivity model of hydrogen injection after 100 days (case 4). (c) Zoomed ERT inversion result after 100 days (case 4). (d) Resistivity model of hydrogen injection after 365 days (case 4). (e) Zoomed ERT inversion result after 365 days (case 4).

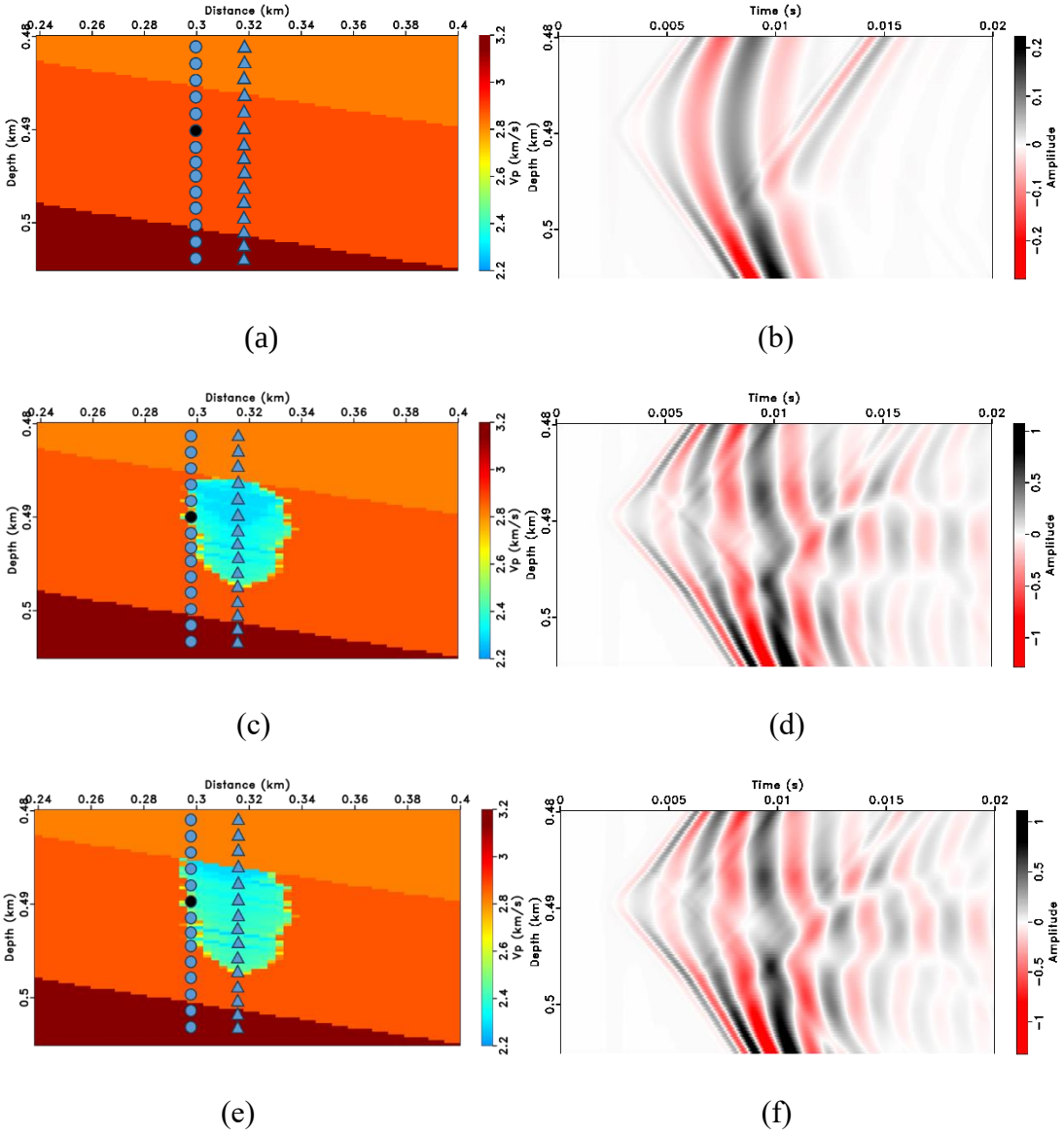

Figure 27. (a) 2D slice of baseline velocity model. (b) Crosshole seismic response corresponding to Figure 27a. (c) 2D slice of velocity model after 100 days (case 4). (d) Crosshole seismic response corresponding to Figure 27c. (e) 2D slice of velocity model after 365 days (case 4). (f) Crosshole seismic response corresponding to Figure 27e.

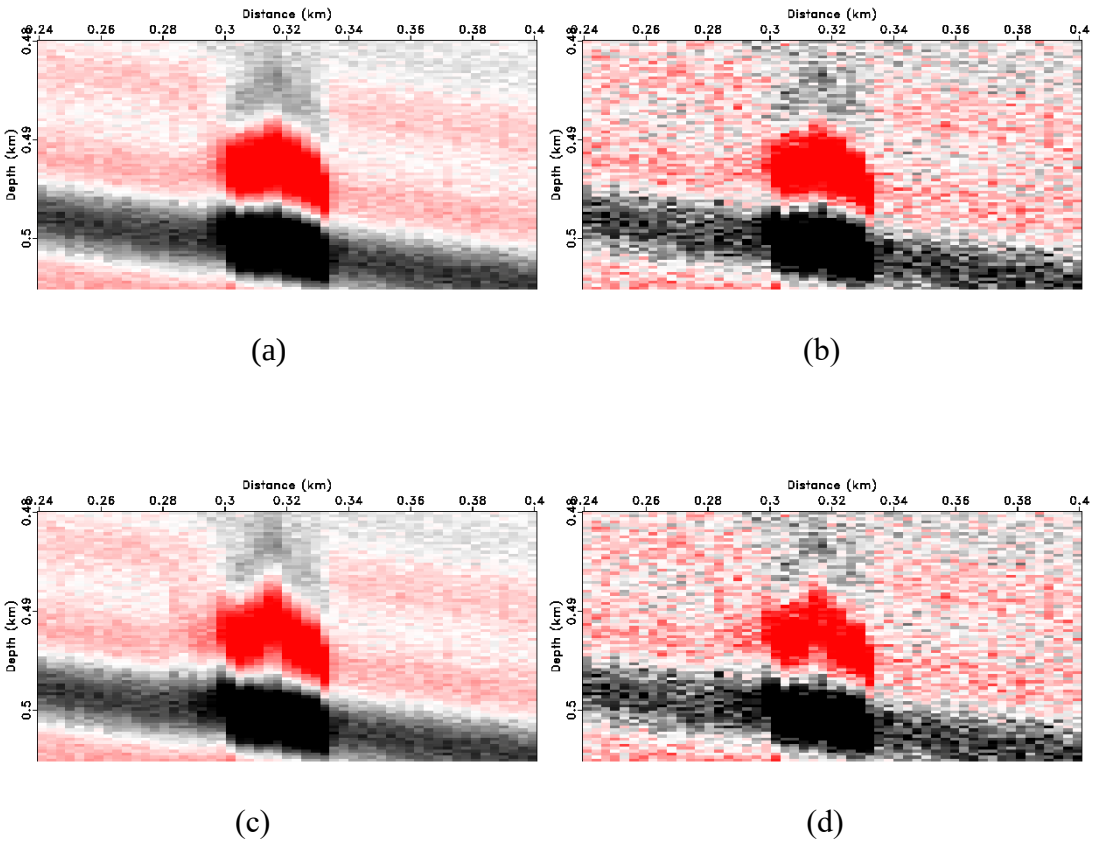

Figure 28. Influence of noise on poststack seismic responses. (a), and (b) are the seismic responses after 100 days with different SNRs (e.g, 3.4 dB, and -6.6 dB). (c), and (d) are the seismic responses after 365 days with different SNRs (e.g, 3.1 dB, and -6.8 dB).

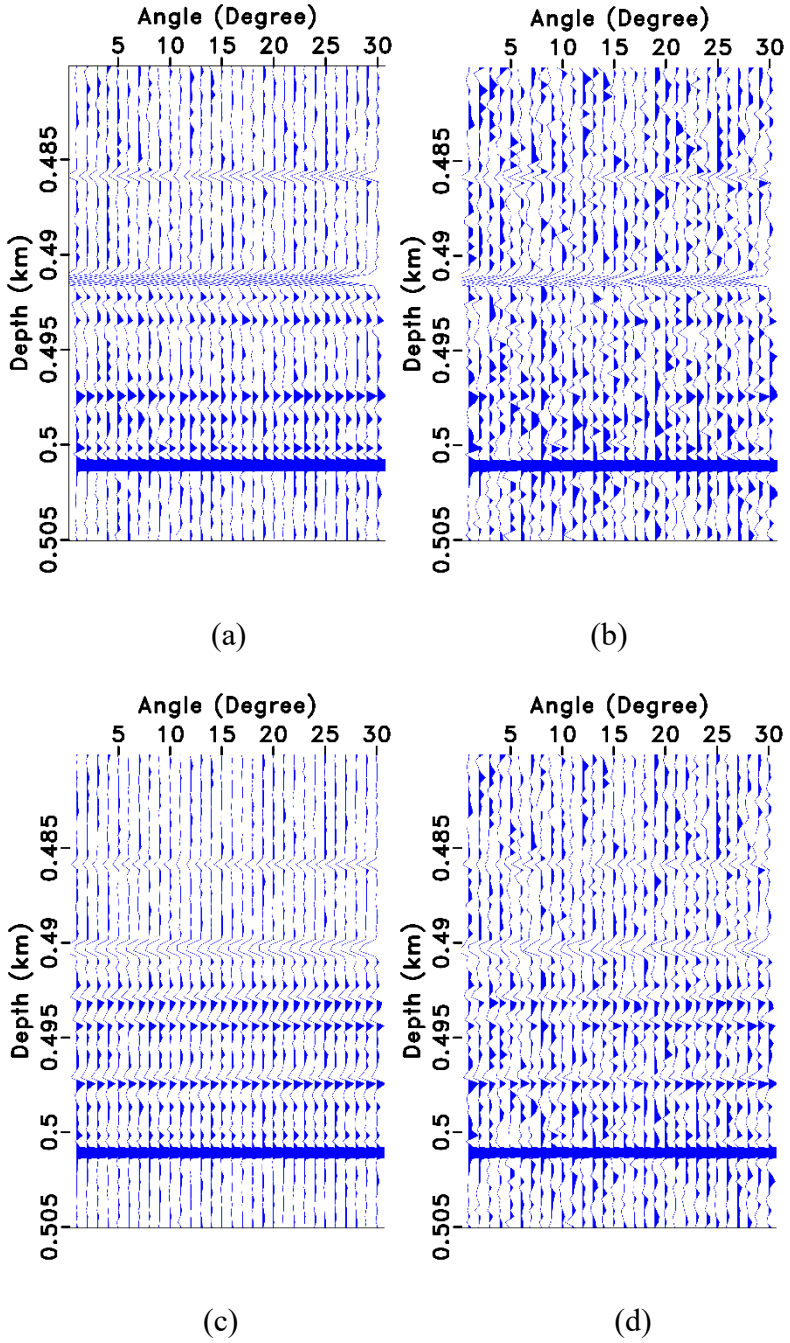

Figure 29. Influence of noise on prestack seismic responses. (a) and (b) are the seismic responses after 100 days with different SNRs (e.g, 5.38 dB and -4.6 dB). (c) and (d) are the seismic responses after 365 days with different SNRs (e.g, 4.9 dB and -5.1 dB).

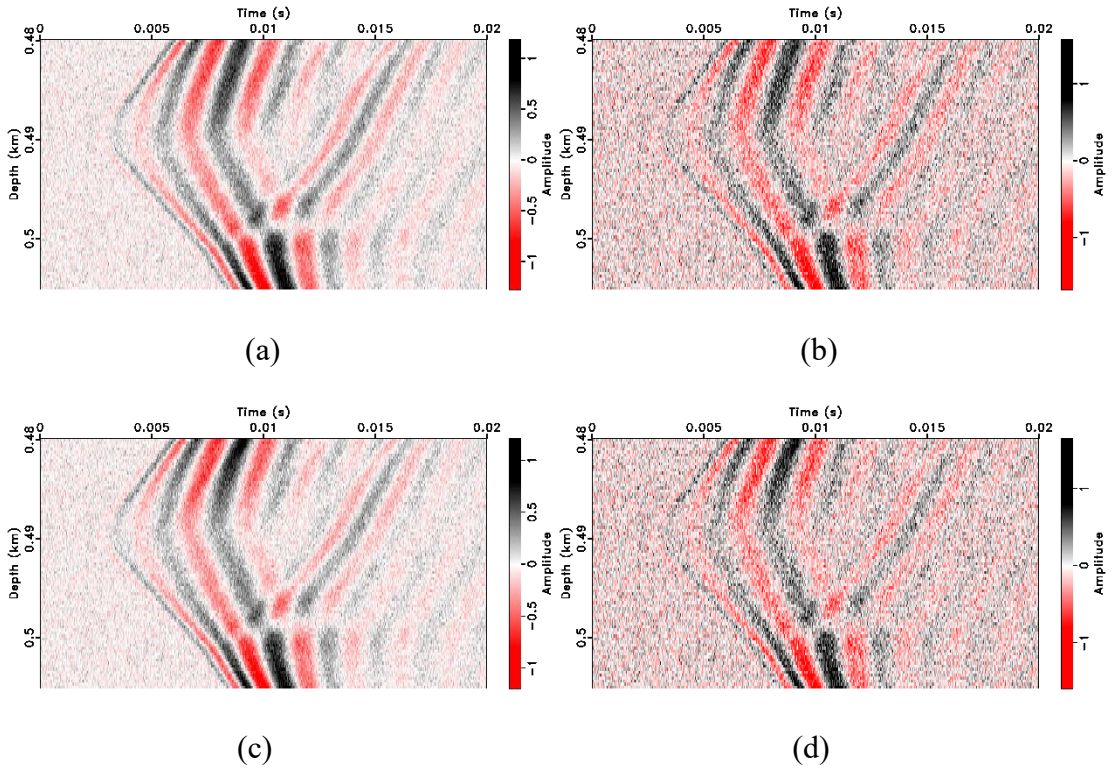

Figure 30. Influence of noise on crosshole seismic responses. (a) and (b) are the seismic responses after 100 days with different SNRs (e.g, 5.4 dB and -1.6 dB). (c) and (d) are the seismic responses after 365 days with different SNRs (e.g, 5 dB and -2 dB).

APPENDIX

I. Madagascar code for rock physics modeling

Our code is mainly based on Madagascar and Matlab. The following code was used in Case 1 and can be reproduced for other cases.

```
# Please consider citing our article if you think the code is helpful for your study.
#Li, C., S. Bhattacharya, M. Alhotan, and M. Delshad and, 2024, Time-lapse geophysical responses of hydrogen-saturated rock: Implications on subsurface monitoring.
from rsf.proj import *
from rsf.recipes.beg import server
from rsf.prog import RSFROOT
##################model building  (4.5MPa and 35°C)
######### the following address needs to be modified as
######## dd='/your address/hydrogen_code/data/case1_time100.rsf'
#########100 days  loading saturation model as time100
dd='/mnt/c/geo_utexas/project/hydrogen/test6192024/hydrogen_code/data/case1_time100.rsf'
Flow('time100all',dd,'transp plane=23|put label1=Z unit1=ft d1=1 d2=10 d3=10 label2=X unit2=ft label3=Y unit3=ft o1=1550 o2=0 o3=0')
Flow('m1','time100all','window n1=1|spray axis=1 n=1550 d=1 o=0|math output=1e-6')###############saturation for top layers
Flow('m3','time100all','window n1=1|spray axis=1 n=100 d=1 o=0|math output=1e-6')###############saturation for bottom layers
Flow('satb100','m1 time100all m3','cat axis=1 ${SOURCES[1:-1]} d=1 o=0 ')
```

```
###############complete saturation before shift
# INITIALIZATION
##########################################################################
matlab        = WhereIs('matlab')
matROOT                                                                    =
'/mnt/c/geo_utexas/project/hydrogen/test6192024/hydrogen_code/Matlab_rock_physics'
matfun = 'property_estimation'
matfun1= 'modelshift'
matlabpath = os.environ.get('MATLABPATH',os.path.join(RSFROOT,'lib'))
if not matlab:
   sys.stderr.write('\nCannot find Matlab.\n')
   sys.exit(1)
####model size
n1=1700
n2=210
n3=216
slp=2.5 ###degree
######### saturation after shift
Flow('sata100',[os.path.join(matROOT,matfun1+'.m'),'satb100'],
    '"MATLABPATH=%(matlabpath)s %(matlab)s
    -nosplash                                  -nojvm                                  -r
"addpath  %(matROOT)s;%(matfun1)s('${SOURCES[1]}','${TARGETS[0]}',%(n1)d,%(n2)d,%(
n3)d,%(slp)g);quit"
```

```
    '"%vars(),stdin=0,stdout=-1)



########################################## porosity model reconstruction before injection
Flow('m1poro','m1','math output=0.08') ###############porosity for top layers
Flow('m3poro','m3','math output=0.04') ###############porosity for bottom layers
Flow('m2poro','time100all','math output=0.2') ###############porosity for reservoir
Flow('porob100','m1poro m2poro m3poro','cat axis=1 ${SOURCES[1:-1]} d=1 o=0')
######### porosity after shift
Flow('poroa100',[os.path.join(matROOT,matfun1+'.m'),'porob100'],
    '"MATLABPATH=%(matlabpath)s %(matlab)s
    -nosplash -nojvm -r
"addpath %(matROOT)s;%(matfun1)s('${SOURCES[1]}','${TARGETS[0]}',%(n1)d,%(n2)d,%(
n3)d,%(slp)g);quit"
    '"%vars(),stdin=0,stdout=-1)
Result('poroa100','window min1=1550|put label1=Z unit1=ft d1=1 d2=10 d3=10 label2=X
unit2=ft label3=Y unit3=ft o1=1550 o2=0 o3=0|byte gainpanel=a bar=bar.rsf |grey3 color=j
frame1=70 frame2=105 frame3=107 scalebar=y flat=n wanttitle=n barlabel=Porosity point1=0.8
point2=0.8')  ####plot
##############################clay fraction model
Flow('m1clay','m1','math output=0.9') ###############clay fraction for top layers
Flow('m3clay','m3','math output=0.9') ###############clay fraction for bottom layers
Flow('m2clay','time100all','math output=0.0') ###############clay fraction for reservoir
```

```
Flow('clayb100','m1clay m2clay m3clay','cat axis=1 ${SOURCES[1:-1]} d=1 o=0')

######### porosity after shift

Flow('claya100',[os.path.join(matROOT,matfun1+'.m'),'clayb100'],

    '''MATLABPATH=%(matlabpath)s %(matlab)s

    -nosplash -nojvm -r

"addpath  %(matROOT)s;%(matfun1)s('${SOURCES[1]}','${TARGETS[0]}',%(n1)d,%(n2)d,%(

n3)d,%(slp)g);quit"

    '''%vars(),stdin=0,stdout=-1)

khy=0.0056  ################bulk modulus of hydrogen under reservoir condition

rhy=0.003   ################density of hydrogen under reservoir condition

le=3 ################patchiness

Flow('vp100 vs100 rho100',[os.path.join(matROOT,matfun+'.m'),'claya100','poroa100','sata100'],

    '''MATLABPATH=%(matlabpath)s %(matlab)s

    -nosplash -nojvm -r

"addpath  %(matROOT)s;%(matfun)s('${SOURCES[1]}','${SOURCES[2]}','${SOURCES[3]}','

${TARGETS[0]}','${TARGETS[1]}','${TARGETS[2]}',%(n1)d,%(n2)d,%(n3)d,%(le)g,%(khy)

g,%(rhy)g);quit"

    '''%vars(),stdin=0,stdout=-1)   #############generate vp, vs, and density models

Flow('imp100','vp100 rho100','math x=${SOURCES[1]} output="input*x*1000"|put

d1=0.0003048 d2=0.003048 d3=0.003048  o1=0 o2=0 o3=0 label1=Depth unit1=km label2=X

unit2=km label3=Y unit3=km ') #############impedance model

################poststack data creation 60 Hz 100 days
```

```
Flow('data100','imp100','ai2refl|ricker1 frequency=60')
Result('data100','put d2=0.003048 d3=0.003048  o2=0 o3=0|window n3=1 f3=107 min1=0.48 max1=0.505 min2=0.24 max2=0.4|grey color=g clip=0.005 wanttitle=n labelsz=8 labelfat=4 font=2 titlesz=10 titlefat=4 label2=Distance unit2=km screenratio=0.5 ')
###################################after 365 days loading saturation model as time365
######### the following address needs to be modified as
######## dd='/your address/hydrogen_code/data/case1_time365.rsf'
dd='/mnt/c/geo_utexas/project/hydrogen/test6192024/hydrogen_code/data/case1_time365.rsf'
Flow('time365all',dd,'transp plane=23|put label1=Z unit1=ft d1=1 d2=10 d3=10 label2=X unit2=ft label3=Y unit3=ft o1=1550 o2=0 o3=0')
Flow('satb365','m1 time365all m3','cat axis=1 ${SOURCES[1:-1]} d=1 o=0 ')
###############saturation before shift 365 days
#########saturation after shift
Flow('sata365',[os.path.join(matROOT,matfun1+'.m'),'satb365'],
    '"MATLABPATH=%(matlabpath)s %(matlab)s
    -nosplash -nojvm -r "addpath %(matROOT)s;%(matfun1)s('${SOURCES[1]}','${TARGETS[0]}',%(n1)d,%(n2)d,%(n3)d,%(slp)g);quit"
    '"%vars(),stdin=0,stdout=-1)
Flow('vp365 vs365 rho365',[os.path.join(matROOT,matfun+'.m'),'claya100','poroa100','sata365'],
    '"MATLABPATH=%(matlabpath)s %(matlab)s
    -nosplash -nojvm -r
```

"addpath %(matROOT)s;%(matfun)s('${SOURCES[1]}','${SOURCES[2]}','${SOURCES[3]}','${TARGETS[0]}','${TARGETS[1]}','${TARGETS[2]}',%(n1)d,%(n2)d,%(n3)d,%(le)g,%(khy)g,%(rhy)g);quit"

'"%vars(),stdin=0,stdout=-1) ##############generate vp, vs, and density models

Flow('imp365','vp365 rho365','math x=${SOURCES[1]} output="input*x*1000"|put d1=0.0003048 d2=0.003048 d3=0.003048 o1=0 o2=0 o3=0 label1=Depth unit1=km label2=X unit2=km label3=Y unit3=km ')

###############poststack data creation 60 Hz 365 days

Flow('data365','imp365','ai2refl|ricker1 frequency=60')

Result('data365','put d2=0.003048 d3=0.003048 o2=0 o3=0|window n3=1 f3=107 min1=0.48 max1=0.505 min2=0.24 max2=0.4|grey color=g clip=0.005 wanttitle=n labelsz=8 labelfat=4 font=2 titlesz=10 titlefat=4 label2=Distance unit2=km screenratio=0.5')

#################################after 0 day loading saturation model as time0

######### the following address needs to be modified as

######## dd='/your address/hydrogen_code/data/case1_time0.rsf'

dd='/mnt/c/geo_utexas/project/hydrogen/test6192024/hydrogen_code/data/case1_time0.rsf'

Flow('time0all',dd,'transp plane=23|put label1=Z unit1=ft d1=1 d2=10 d3=10 label2=X unit2=ft label3=Y unit3=ft o1=1550 o2=0 o3=0')

Flow('satb0','m1 time0all m3','cat axis=1 ${SOURCES[1:-1]} d=1 o=0 ')

###############saturation before shift 0 day

######### saturation after shift

Flow('sata0',[os.path.join(matROOT,matfun1+'.m'),'satb0'],

'"MATLABPATH=%(matlabpath)s %(matlab)s

-nosplash -nojvm -r "addpath %(matROOT)s;%(matfun1)s('${SOURCES[1]}','${TARGETS[0]}',%(n1)d,%(n2)d,%(n3)d,%(slp)g);quit"

"'%vars(),stdin=0,stdout=-1)

Flow('vp0 vs0 rho0',[os.path.join(matROOT,matfun+'.m'),'claya100','poroa100','sata0'],

"'MATLABPATH=%(matlabpath)s %(matlab)s

-nosplash -nojvm -r "addpath %(matROOT)s;%(matfun)s('${SOURCES[1]}','${SOURCES[2]}','${SOURCES[3]}','${TARGETS[0]}','${TARGETS[1]}','${TARGETS[2]}',%(n1)d,%(n2)d,%(n3)d,%(le)g,%(khy)g,%(rhy)g);quit"

"'%vars(),stdin=0,stdout=-1) ####vp, vs, density estimation after 0 day

Flow('imp0','vp0 rho0','math x=${SOURCES[1]} output="input*x*1000"|put d1=0.0003048 d2=0.003048 d3=0.003048 o1=0 o2=0 o3=0 label1=Depth unit1=km label2=X unit2=km label3=Y unit3=km ')

################poststack data creation 60 Hz 365 days

Flow('data0','imp0','ai2refl|ricker1 frequency=60 ')

Result('data0','put d2=0.003048 d3=0.003048 o2=0 o3=0|window n3=1 f3=107 min1=0.48 max1=0.505 min2=0.24 max2=0.4|grey color=g clip=0.005 wanttitle=n labelsz=8 labelfat=4 font=2 titlesz=10 titlefat=4 label2=Distance unit2=km screenratio=0.5')

##resitivity model after 100 days and 365 days using Archie equation

Flow('res100','sata100','sfput d1=0.0003048 d2=0.003048 d3=0.003048 o1=0 o2=0 o3=0 unit1=km unit2=km unit3=km label1=Depth label2=Distance label3=Y|sfwindow n3=1

f3=107|sfwindow min1=0.48 max1=0.505|sfmath output="1-input"|sfmath output="input*input"|sfmath output="0.04/input/0.04" |window min2=0.24 max2=0.4')

Result('res100','grey color=j scalebar=y bias=10 wanttitle=n barunit="Ohm.m" barlabel=Resistivity screenratio=0.5 labelsz=8 labelfat=4 font=2 titlesz=10 titlefat=4')

Flow('res365','sata365','sfput d1=0.0003048 d2=0.003048 d3=0.003048 o1=0 o2=0 o3=0 unit1=km unit2=km unit3=km label1=Depth label2=Distance label3=Y|sfwindow n3=1 f3=107|sfwindow min1=0.48 max1=0.505|sfmath output="1-input"|sfmath output="input*input"|sfmath output="0.04/input/0.04" |window min2=0.24 max2=0.4')

Result('res365','grey color=j scalebar=y bias=10 wanttitle=n barunit="Ohm.m" barlabel=Resistivity screenratio=0.5 labelsz=8 labelfat=4 font=2 titlesz=10 titlefat=4')

##zoomed resitivity model after 100 days

Flow('sres100','sata100','sfput d1=0.0003048 d2=0.003048 d3=0.003048 o1=0 o2=0 o3=0 unit1=km unit2=km unit3=km label1=Depth label2=Distance label3=Y|sfwindow n3=1 f3=107|sfwindow min2=0.312 max2=0.317 min1=0.49 max1=0.499|sfmath output="1-input"|sfmath output="input*input"|sfmath output="0.04/input/0.04" '

Result('sres100','grey color=j scalebar=y bias=10 wanttitle=n barunit="Ohm.m" barlabel=Resistivity screenratio=1.5 labelsz=8 labelfat=4 font=2 titlesz=10 titlefat=4')

##zoomed resitivity model after 365 days

Flow('sres365','sata365','sfput d1=0.0003048 d2=0.003048 d3=0.003048 o1=0 o2=0 o3=0 unit1=km unit2=km unit3=km label1=Depth label2=Distance label3=Y|sfwindow n3=1 f3=107|sfwindow min2=0.312 max2=0.317 min1=0.49 max1=0.499|sfmath output="1-input"|sfmath output="input*input"|sfmath output="0.04/input/0.04" ')

Result('sres365','grey color=j scalebar=y bias=8 wanttitle=n barunit="Ohm.m"

barlabel=Resistivity screenratio=1.5 labelsz=8 labelfat=4 font=2 titlesz=10 titlefat=4 ')

##resitivity model after 0 day

Flow('sres0','sata0','sfput d1=0.0003048 d2=0.003048 d3=0.003048 o1=0 o2=0 o3=0 unit1=km unit2=km unit3=km label1=Depth label2=Distance label3=Y|sfwindow n3=1 f3=107|sfwindow min1=0.48 max1=0.505|sfmath output="1-input"|sfmath output="input*input"|sfmath output="0.04/input/0.04"|window min2=0.24 max2=0.4 ')

Result('sres0','grey color=j scalebar=y bias=10 wanttitle=n barunit="Ohm.m" barlabel=Resistivity screenratio=0.5 labelsz=8 labelfat=4 font=2 titlesz=10 titlefat=4 ')

#####################################**AVO forward for case1**

INITIALIZATION

##

matlab = WhereIs('matlab')

matROOT = '/mnt/c/geo_utexas/project/hydrogen/test6192024/hydrogen_code/Matlab_rock_physics'

matfun2 = 'seis_ava'

matlabpath = os.environ.get('MATLABPATH',os.path.join(RSFROOT,'lib'))

if not matlab:

    sys.stderr.write('\nCannot find Matlab.\n')

    sys.exit(1)

###2D slices of saturation model

Flow('tsata0','sata0','put d1=0.0003048 d2=0.003048 d3=0.003048 o1=0 o2=0 o3=0|window n3=1 f3=107 min1=0.48 max1=0.505 min2=0.24 max2=0.4 ') ###2D slices saturation 0 day

Flow('tsata100','sata100','put d1=0.0003048 d2=0.003048 d3=0.003048 o1=0 o2=0 o3=0|window

n3=1 f3=107 min1=0.48 max1=0.505 min2=0.24 max2=0.4 ') ###2D slices saturation 100 day

Flow('tsata365','sata365','put d1=0.0003048 d2=0.003048 d3=0.003048 o1=0 o2=0 o3=0|window n3=1 f3=107 min1=0.48 max1=0.505 min2=0.24 max2=0.4 ') ###2D slices saturation 365 days

Result('tsata0','grey color=j scalebar=y bias=0.1 barlabel=Saturation wanttitle=n label1=Depth unit1=km label2=Distance unit2=km labelsz=8 labelfat=4 font=2 titlesz=10 titlefat=4 screenratio=0.5 allpos=y')

Result('tsata100','grey color=j scalebar=y bias=0.4 barlabel=Saturation wanttitle=n label1=Depth unit1=km label2=Distance unit2=km labelsz=8 labelfat=4 font=2 titlesz=10 titlefat=4 screenratio=0.5')

Result('tsata365','grey color=j scalebar=y bias=0.4 barlabel=Saturation wanttitle=n label1=Depth unit1=km label2=Distance unit2=km labelsz=8 labelfat=4 font=2 titlesz=10 titlefat=4 screenratio=0.5')

###**2D slices of models**

Flow('mvp0','vp0','put d1=0.0003048 d2=0.003048 d3=0.003048 o1=0 o2=0 o3=0|window n3=1 f3=107 min1=0.48 max1=0.505 min2=0.24 max2=0.4 ') ###2D slices vp 0 day

Flow('mvp100','vp100','put d1=0.0003048 d2=0.003048 d3=0.003048 o1=0 o2=0 o3=0|window n3=1 f3=107 min1=0.48 max1=0.505 min2=0.24 max2=0.4 ')###2D slices 100 days

Flow('mvp365','vp365','put d1=0.0003048 d2=0.003048 d3=0.003048 o1=0 o2=0 o3=0|window n3=1 f3=107 min1=0.48 max1=0.505 min2=0.24 max2=0.4 ')###2D slices 365 days

Result('mvp0','grey color=j scalebar=y bias=2.5 barlabel=Vp barunit=km/s wanttitle=n label1=Depth unit1=km label2=Distance unit2=km labelsz=8 labelfat=4 font=2 titlesz=10 titlefat=4 screenratio=0.5 ')

Result('mvp100','grey color=j scalebar=y bias=2.5 barlabel=Vp barunit=km/s wanttitle=n

label1=Depth unit1=km label2=Distance unit2=km labelsz=8 labelfat=4 font=2 titlesz=10 titlefat=4 screenratio=0.5 ')

Result('mvp365','grey color=j scalebar=y bias=2.5 barlabel=Vp barunit=km/s wanttitle=n label1=Depth unit1=km label2=Distance unit2=km labelsz=8 labelfat=4 font=2 titlesz=10 titlefat=4 screenratio=0.5')

############################**Extract model for prestack forward modeling**

Flow('tvp0','vp0','put d1=0.0003048 d2=0.003048 d3=0.003048 o1=0 o2=0 o3=0|window n3=1 f3=107|window n2=1 min2=0.317') ###single vp 0 day

Flow('tvs0','vs0','put d1=0.0003048 d2=0.003048 d3=0.003048 o1=0 o2=0 o3=0|window n3=1 f3=107|window n2=1 min2=0.317') ###single vs 100 day

Flow('trho0','rho0','put d1=0.0003048 d2=0.003048 d3=0.003048 o1=0 o2=0 o3=0|window n3=1 f3=107|window n2=1 min2=0.317') ###single rho 100 day

Flow('tvp100','vp100','put d1=0.0003048 d2=0.003048 d3=0.003048 o1=0 o2=0 o3=0|window n3=1 f3=107|window n2=1 min2=0.317') ###single vp 100 day

Flow('tvs100','vs100','put d1=0.0003048 d2=0.003048 d3=0.003048 o1=0 o2=0 o3=0|window n3=1 f3=107|window n2=1 min2=0.317') ###single vs 100 day

Flow('trho100','rho100','put d1=0.0003048 d2=0.003048 d3=0.003048 o1=0 o2=0 o3=0|window n3=1 f3=107|window n2=1 min2=0.317') ###single rho 100 day

Flow('tvp365','vp365','put d1=0.0003048 d2=0.003048 d3=0.003048 o1=0 o2=0 o3=0|window n3=1 f3=107|window n2=1 min2=0.317') ###single vp 365 day

Flow('tvs365','vs365','put d1=0.0003048 d2=0.003048 d3=0.003048 o1=0 o2=0 o3=0|window n3=1 f3=107|window n2=1 min2=0.317') ###single vs 100 day

Flow('trho365','rho365','put d1=0.0003048 d2=0.003048 d3=0.003048 o1=0 o2=0 o3=0|window

```
n3=1 f3=107|window n2=1 min2=0.317') ###single rho 100 day


n1=1700  #######number of samples in the first axis
n2=1     #######number of samples in the second axis
mintheta=1
maxtheta=30 #######begin from 1 to 30 degree
Flow('refl0',[os.path.join(matROOT,matfun2+'.m'),'tvp0','tvs0','trho0'],
    '"MATLABPATH=%(matlabpath)s %(matlab)s
    -nosplash                                    -nojvm                                    -r
"addpath %(matROOT)s;%(matfun2)s('${SOURCES[1]}','${SOURCES[2]}','${SOURCES[3]}',
'${TARGETS[0]}',%(n1)d,%(n2)d,%(mintheta)g,%(maxtheta)g);quit"
    '"%vars(),stdin=0,stdout=-1)  #######prestack reflectivity series 0 day
Flow('refl100',[os.path.join(matROOT,matfun2+'.m'),'tvp100','tvs100','trho100'],
    '"MATLABPATH=%(matlabpath)s %(matlab)s
    -nosplash                                    -nojvm                                    -r
"addpath %(matROOT)s;%(matfun2)s('${SOURCES[1]}','${SOURCES[2]}','${SOURCES[3]}',
'${TARGETS[0]}',%(n1)d,%(n2)d,%(mintheta)g,%(maxtheta)g);quit"
    '"%vars(),stdin=0,stdout=-1)  ######prestack reflectivity series 100 days
Flow('refl365',[os.path.join(matROOT,matfun2+'.m'),'tvp365','tvs365','trho365'],
    '"MATLABPATH=%(matlabpath)s %(matlab)s
    -nosplash                                    -nojvm                                    -r
"addpath %(matROOT)s;%(matfun2)s('${SOURCES[1]}','${SOURCES[2]}','${SOURCES[3]}',
'${TARGETS[0]}',%(n1)d,%(n2)d,%(mintheta)g,%(maxtheta)g);quit"
```

"'%vars(),stdin=0,stdout=-1) ######prestack reflectivity series 365 days

############**Plot**

Result('mref0','refl0','sfput d1=0.0003048 d2=1 o1=0 o2=1 |sfwindow min1=0.48 max1=0.505|sfwiggle transp=y yreverse=y poly=y grid=n wanttitle=n label1=Depth unit1=km label2=Angle unit2=Degree screenratio=1.5 wherexlabel=top labelsz=8 labelfat=4 font=2 titlesz=10 titlefat=4')

Result('mref100','refl100','sfput d1=0.0003048 d2=1 o1=0 o2=1 |sfwindow min1=0.48 max1=0.505|sfwiggle transp=y yreverse=y poly=y pclip=95 grid=n wanttitle=n label1=Depth unit1=km label2=Angle unit2=Degree screenratio=1.5 wherexlabel=top labelsz=8 labelfat=4 font=2 titlesz=10 titlefat=4 zplot=0.4')

Result('mref365','refl365','sfput d1=0.0003048 d2=1 o1=0 o2=1 |sfwindow min1=0.48 max1=0.505|sfwiggle transp=y yreverse=y poly=y pclip=95 grid=n wanttitle=n label1=Depth unit1=km label2=Angle unit2=Degree screenratio=1.5 wherexlabel=top labelsz=8 labelfat=4 font=2 titlesz=10 titlefat=4')

##############################**NRMS calculation, please refer to Kragh and Christie**

Flow('tdata0',' data0',' sfput d2=0.003048 d3=0.003048 o2=0 o3=0|window n3=1 f3=107 min1=0.48 max1=0.505 min2=0.24 max2=0.4')

Flow('tdata100','data100','sfput d2=0.003048 d3=0.003048 o2=0 o3=0|window n3=1 f3=107 min1=0.48 max1=0.505 min2=0.24 max2=0.4')

Flow('tdata365','data365','sfput d2=0.003048 d3=0.003048 o2=0 o3=0|window n3=1 f3=107 min1=0.48 max1=0.505 min2=0.24 max2=0.4')

```
Flow('coef0','tdata0','math output="input*input"|stack axis=2|math output="sqrt(input)"')
Flow('coef100','tdata100','math output="input*input"|stack axis=2|math output="sqrt(input)"')
Flow('coef365','tdata365','math output="input*input"|stack axis=2|math output="sqrt(input)"')

Flow('coefd100','tdata0 tdata100','math x=${SOURCES[1]} output="input-x"|math output="input*input"|stack axis=2|math output="sqrt(input)"')
Flow('coefd365','tdata0 tdata365','math x=${SOURCES[1]} output="input-x"|math output="input*input"|stack axis=2|math output="sqrt(input)"')
Flow('nrms100','coefd100 coef0 coef100','math x=${SOURCES[1]} y=${SOURCES[2]} output="200*input/(x+y)"|stack axis=1')####NRMS after 100 days
Flow('nrms365','coefd365 coef0 coef365','math x=${SOURCES[1]} y=${SOURCES[2]} output="200*input/(x+y)"|stack axis=1')####NRMS after 365 days
##############################NRMS calculation for ERT
Flow('coef0ert','sres0','math output="input*input"|stack axis=2|math output="sqrt(input)"')
Flow('coef100ert','res100','math output="input*input"|stack axis=2|math output="sqrt(input)"')
Flow('coef365ert','res365','math output="input*input"|stack axis=2|math output="sqrt(input)"')
Flow('coefd100ert','sres0 res100','math x=${SOURCES[1]} output="input-x"|math output="input*input"|stack axis=2|math output="sqrt(input)"')
Flow('coefd365ert','sres0 res365','math x=${SOURCES[1]} output="input-x"|math output="input*input"|stack axis=2|math output="sqrt(input)"')
Flow('nrms100ert','coefd100ert coef0ert coef100ert','math x=${SOURCES[1]} y=${SOURCES[2]} output="200*input/(x+y)"|stack axis=1')####NRMS after 100 days
Flow('nrms365ert','coefd365ert coef0ert coef365ert','math x=${SOURCES[1]}
```

```
y=${SOURCES[2]} output="200*input/(x+y)"|stack axis=1')####NRMS after 365 days
End()
```

II. Matlab functions used for rock physics forward modeling

```
function modelshift(infile1,outfile,n1,n2,n3,slp)
%%%%%%%%%%aim to move model along a fixed degree
%%%%%%%% infile1:model
%%%%%%%% n1:the first dimension
%%%%%%%% n2:the second dimension
%%%%%%%% n3:the third dimension
%%%%%%%% slp: dip in degree
m=zeros(n1,n2,n3);
rsf_read(m,infile1);
rsf_create(outfile,[n1,n2,n3]');
m1=m;


x1=(0:n2-1).*10;
loc=round(tan(2.5/180*3.1415926)*x1/1);
for j=1:n3
  for i=1:n2
     trc=m(:,i,j);
     m1(loc(i)+1:end,i,j)=trc(1:n1-loc(i));   %%%%%%%%%%model moving
  end
```

```
end
rsf_write(m1,outfile);  %%%%%%%%%%%output
end

%%rock physics forward modeling
function property_estimation(infile1,infile2,infile3,outfile1,outfile2,outfile3,n1,n2,n3,le,khy,rhy)
%%%%%%%% infile1: clay fraction
%%%%%%%% infile2: porosity
%%%%%%%% infile3: hydrogen saturation
%%%%%%%% le: patchness exponent
%%%%%%%% outfile1: vp
%%%%%%%% outfile2: vs
%%%%%%%% outfile3: rho
clay=zeros(n1,n2,n3);

poro=zeros(n1,n2,n3);
sathy=zeros(n1,n2,n3);
sn=zeros(n1,n2,n3);
%%%%%%%%%%%%input loading
rsf_read(clay,infile1);
rsf_read(poro,infile2);
rsf_read(sathy,infile3);
vpmodel=zeros(n1,n2,n3);
```

```
vsmodel=zeros(n1,n2,n3);
rhomodel=zeros(n1,n2,n3);
%%%begin calculation
for k=1:n3
  for j=1:n2
   for i=1:n1
       outa=rock_forward(clay(i,j,k),poro(i,j,k),sathy(i,j,k),le,khy,rhy);
       vpmodel(i,j,k)=outa(1);
       vsmodel(i,j,k)=outa(2);
       rhomodel(i,j,k)=outa(3);
   end
  end
end
%%%%%%%output creation
rsf_create(outfile1,[n1,n2,n3]')
rsf_create(outfile2,[n1,n2,n3]')
rsf_create(outfile3,[n1,n2,n3]')
%%%%%%%%data output
rsf_write(vpmodel,outfile1);
rsf_write(vsmodel,outfile2);
rsf_write(rhomodel,outfile3);
end
```

```
%rock physics forwarding to generate vp, vs, and density
function outa=rock_forward(fravsh,porosity,shy,e,khy,rhy)
%%%%% shy: hydrogen saturation
%%%%% if possible we can change volume fraction of shale and quartz
%%%%% fravsh: clay fraction
%%%%% output outa=[vp,vs,rho]
%%%%% khy: bulk modulus of hydrogen rhy: density of hydrogen
sg=shy;
phi=porosity;
vsh = fravsh; %%% clay fraction
sand = 1-vsh;  %%% sand fraction
sw = 1-sg;%%% water satuation
%%% elastic modulus
k1 = 39.0;   u1 = 45.0; rho1 = 2.65; v1 = sand; %quartz
k2 = 21;     u2 = 6.85; rho2 = 2.6 ; v2 = vsh; %clay
k3 = khy;    u3 = 0.00; rho3 = rhy;  v3 = phi.*sg; %hydrogen
k4 = 2.49;   u4 = 0.00; rho4 = 1.03; v4 = phi.*sw; %water
%%%% VRH average
k_temp = [k1; k2];
u_temp = [u1; u2]; all_temp = v1+v2;
v_temp = [v1/all_temp; v2/all_temp];
k_vrh = (sum(v_temp.*k_temp)+1/sum(v_temp./k_temp))/2;
u_vrh = (sum(v_temp.*u_temp)+1/sum(v_temp./u_temp))/2;
```

```
%%%% Hertz mandlin model
poisson=(3*k_vrh-2*u_vrh)/(6*k_vrh+2*u_vrh); %%% poisson ratio estimation
phic=0.36;  %%%%critical porosity
C=2.8/phic; %%%% average number of contacts
peff=2250*9.8*470/1000/1000/1000; %%%%%%%%%%effective pressure
kc=((C*C*(1-phic)^2*u_vrh^2*peff)/(18*3.1415*3.1415*(1-poisson)^2))^(1/3);  %%%%critical bulk modulus
uc=((5-4*poisson)/(10-5*poisson))*((3*C*C*(1-phic)^2*u_vrh^2*peff)/(2*3.1415*3.1415*(1-poisson)^2))^(1/3);  %%%%%critical shear modulus
xi=(uc/6)*(9*kc+8*uc)/(kc+2*uc);
kdry=(((phi/phic)/(kc+4/3*uc))+((1-phi/phic)/(k_vrh+4/3*uc)))^(-1)-4/3*uc;     %%%dry frame bulk modulus
udry=(((phi/phic)/(uc+xi))+((1-phi/phic)/(u_vrh+xi)))^(-1)-xi; %%%dry frame shear modulus
k_f=(k4-k3)*sw^(e)+k3;     %%%%%brine+hydrogen  k4 brine  k3 hydrogen using brie's equation
%% denstiy calculation
rho = [rho1;rho2;rho3;rho4];
all_temp = 1;
v = [(1-phi)*v1/all_temp;(1-phi)*v2/all_temp;v3./all_temp;v4./all_temp];
rho_sat = sum(v.*rho);
%% ksat calculation
phi_temp = phi;
k_sat = gassmann(kdry,k_f,k_vrh,phi_temp);
```

```
u_sat = udry;
%%%velocity estimation
vp=sqrt((k_sat+4/3*u_sat)/rho_sat);
vs=sqrt(u_sat/rho_sat);
outa=[vp,vs,rho_sat];
end

%%%%%%Gassmann fluid substitution
function ksat=gassmann(kdry,kfl,ko,phi)
%%%kdry bulk modulus of rock
%%%kfl bulk modulus of fluid
%%%ko  bulk modulus of rock matrix
%%% phi porosity
k1=(1-kdry/ko)^2;
k2=phi/kfl+(1-phi)/ko-kdry/ko/ko;
ksat=kdry+k1/k2;
end

%used for prestack AVA forwarding
function seis_ava(infile1,infile2,infile3,outfile1,n1,n2,mintheta,maxtheta)
%%%%%%%% infile1:vp
%%%%%%%% infile2:vs
%%%%%%%% infile3:rho
```

```
%%%%%%%% mintheta: minimum of theta
%%%%%%%% maxtheta: maximum of theta
%%%%%%%% outfile1:refl reflectivity series
vp=zeros(n1,n2);
vs=zeros(n1,n2);
rho=zeros(n1,n2);
theta=mintheta:1:maxtheta;
ntheta=length(theta);
refl=zeros(n1-1,ntheta,n2);  %%%%prestack reflectivity series
%%%%%%%% data reading
rsf_read(vp,infile1);
rsf_read(vs,infile2);
rsf_read(rho,infile3);
for i=1:n2
   for k=theta
      for j=1:n1-1
         refl(j,k,i)=preava(vp(j,i),vs(j,i),rho(j,i),vp(j+1,i),vs(j+1,i),rho(j+1,i),k,4);   %%call preava
to genernate prestack AVA response.
   end
end
rsf_create(outfile1,[n1-1,ntheta,n2]')  %%%%%%%%%%%%%%%%%%output create
rsf_write(refl,outfile1);%%%%%%%%%%%%%%%%%%output
end
```

```
function Rpp=preava(vp1,vs1,d1,vp2,vs2,d2,ang,approx)
%Calculates P-to-P reflectivity (Rpp) as a function of the angle of incidence (ang).
%input parameters:
%  layer 1 (top): vp1, vs1, density1 (d1)
%  layer 2 (bottom): vp2, vs2, density2 (d2)
% ang: vector with angles(DEG)
% approx: 1)Full Zoeppritz(A&R)
%          2)Aki&Richards
%         3)Shuey's paper
%         4)Castagna's paper->Shuey (slightly different formulation of Shuey)
% With no output arguments, plots Rpp vs. angle.
t=ang.*pi./180;          p=sin(t)./vp1;  ct=cos(t);
da=(d1+d2)/2;     Dd=(d2-d1);
vpa=(vp1+vp2)/2;  Dvp=(vp2-vp1);
vsa=(vs1+vs2)/2;  Dvs=(vs2-vs1);
switch approx
  case 1,                  %FULL Zoeppritz (A&K)
        ct2=sqrt(1-(sin(t).^2.*(vp2.^2./vp1.^2)));
        cj1=sqrt(1-(sin(t).^2.*(vs1.^2./vp1.^2)));
        cj2=sqrt(1-(sin(t).^2.*(vs2.^2./vp1.^2)));
        a=(d2.*(1-(2.*vs2.^2.*p.^2)))-(d1.*(1-(2.*vs1.^2.*p.^2)));
        b=(d2.*(1-(2.*vs2.^2.*p.^2)))+(2.*d1.*vs1.^2.*p.^2);
```

```
        c=(d1.*(1-(2.*vs1.^2.*p.^2)))+(2.*d2.*vs2.^2.*p.^2);
        d=2.*((d2.*vs2.^2)-(d1.*vs1.^2));
        E=(b.*ct./vp1)+(c.*ct2./vp2);
        F=(b.*cj1./vs1)+(c.*cj2./vs2);
        G=a-(d.*ct.*cj2./(vp1.*vs2));
        H=a-(d.*ct2.*cj1./(vp2.*vs1));
        D=(E.*F)+(G.*H.*p.^2);
        Rpp=( (((b.*ct./vp1)-(c.*ct2./vp2)).*F) - ...
        ((a+(d.*ct.*cj2./(vp1.*vs2))).*H.*p.^2) ) ./ D;
  case 2,                   %Aki & Richard (aprox)
%assuming (angles) i=i1
        Rpp=(0.5.*(1-(4.*p.^2.*vsa.^2)).*Dd./da) + (Dvp./(2.*ct.^2.*vpa)) - ...
          (4.*p.^2.*vsa.*Dvs);
  case 3,                   %Shuey
        poi1=((0.5.*(vp1./vs1).^2)-1)./((vp1./vs1).^2-1);
        poi2=((0.5.*(vp2./vs2).^2)-1)./((vp2./vs2).^2-1);
        poia=(poi1+poi2)./2;   Dpoi=(poi2-poi1);
        Ro=0.5.*((Dvp./vpa)+(Dd./da));
        Bx=(Dvp./vpa)./((Dvp./vpa)+(Dd./da));
        Ax=Bx-(2.*(1+Bx).*(1-2.*poia)./(1-poia));
        Rpp= Ro + (((Ax.*Ro)+(Dpoi./(1-poia).^2)).*sin(t).^2) + ...
              (0.5.*Dvp.*(tan(t).^2-sin(t).^2)./vpa);
  case 4,                   %Shuey linear
```

```
        A=0.5.*((Dvp./vpa)+(Dd./da));
        B=(-2.*vsa.^2.*Dd./(vpa.^2.*da)) + (0.5.*Dvp./vpa) - ...
          (4.*vsa.*Dvs./(vpa.^2));
        Rpp=A+(B.*sin(t).^2);
   otherwise,
end
end
```